J. Fluid Mech. (2007), *vol.* 578, *pp.* 139–169.
doi:10.1017/S0022112007005022 Printed in the United Kingdom

The effect of streamwise vortices on the aeroacoustics of a Mach 0.9 jet

MEHMET B. ALKISLAR[1]†, A. KROTHAPALLI[1] AND G. W. BUTLER[2]

[1]Department of Mechanical Engineering, 2525 Pottsdamer Street, Florida A&M University and Florida State University, Tallahassee, FL 32310, USA

[2]The Boeing Company, PO Box 3307 MC ML-67, Seattle, WA 98124, USA

(Received 8 June 2006 and in revised form 20 November 2006)

The role of the streamwise vortices on the aeroacoustics of a Mach 0.9 axisymmetric jet is investigated using two different devices to generate streamwise vortices: microjets and chevrons. The resultant acoustic field is mapped by sideline microphones and a microphone phased array. The flow-field characteristics within the first few diameters of the nozzle exit are obtained using stereoscopic particle image velocimetry (PIV). The flow-field measurements reveal that the counter-rotating streamwise vortex pairs generated by microjets are located primarily at the high-speed side of the initial shear layer. In contrast, the chevrons generate vortices of greater strength that reside mostly on the low-speed side. Although the magnitude of the chevron's axial vorticity is initially higher, it decays more rapidly with downstream distance. As a result, their influence is confined to a smaller region of the jet. The axial vorticity generated by both devices produces an increase in local entrainment and mixing, increasing the near-field turbulence levels. It is argued that the increase in high-frequency sound pressure levels (SPL) commonly observed in the far-field noise spectrum is due to the increase in the turbulence levels close to the jet exit on the high-speed side of the shear layer. The greater persistence and lower strength of the streamwise vortices generated by microjets appear to shift the cross-over frequencies to higher values and minimize the high-frequency lift in the far-field spectrum. The measured overall sound pressure level (OASPL) shows that microjet injection provides relatively uniform noise suppression for a wider range of sound radiation angles when compared to that of a chevron nozzle.

1. Introduction

Much of the work on turbulent subsonic jets over the last few decades has established that large-scale eddies dominate the flow in the region from the nozzle exit to about two potential core lengths, generally referred to as the noise-producing region. The existence of these structures at high Reynolds numbers were shown by Brown & Roshko (1974) in their work on planar free shear layers. In their incompressible round-jet-flow experiments, Crow & Champagne (1971) demonstrated that large-scale orderly structures may be strongly amplified at Strouhal numbers of 0.3, and identified this phenomenon as the preferred mode of the jet column. Although much more difficult, it is still possible to identify large-scale structures in

† Present address: The Boeing Company, PO Box 3307 MC ML-67, Seattle, WA 98124, USA. mehmet.b.alkislar@boeing.com.

higher-Reynolds-number flows, especially when conditional sampling techniques are used. In spite of their apparent dominance in the noise-producing region, a direct relationship between these structures and the sound field is still elusive in subsonic jets.

It is now established that the large eddies are a manifestation of the inherent instability of the jet's initial shear layer (for relevant references on this topic, see Arakeri *et al.* 2003). The acoustic forcing of a high-Reynolds-number turbulent jet (Moore 1977) clearly showed that the presence of the large eddies increases the far-field noise, albeit limited in magnitude to about 5 dB. This phenomenon is also known as the amplification of broadband noise by tonal excitation. Although the mechanism is not well understood, the results are consistent for jets with Reynolds numbers in excess of 5×10^5 (Crighton 1981).

A novel experimental study to determine the direct connection between the large-scale structures and the radiated noise field was carried out by Coiffet (2006) using conditional sampling techniques in conjunction with a near-field linear microphone array and laser doppler velocimetry (LDV). The velocity and near-field pressure correlations clearly identify the relationship between the large-scale eddies and the associated sound field. The maximum correlation coefficient is obtained with the noise sources located at 3 diameters downstream of the exit. Additionally, it was found that the dominant noise sources are located on the high-speed side of the shear layer, consistent with the observation of Alkislar, Krothapalli & Lourenco (2003).

These observations suggest that it should be possible to reduce the jet noise by the disruption of large-scale coherent structure growth – a topic that has received significant attention during the last two decades. With the continuing emphasis on noise reduction techniques that do not significantly interfere with the flow, chevron nozzles have received much attention (Bridges, Wernet & Brown 2003; Saiyed, Mikkelsen & Bridges 2003; Bridges & Brown 2004). Another technique that seems to show much promise is the application of high-pressure microjet injection at or near the nozzle exit (Arakeri *et al.* 2003; Greska *et al.* 2005). These studies have shown a modest reduction in the overall sound pressure level (OASPL) and decrease in shear-layer turbulence levels.

It has also been shown that both techniques introduce streamwise vortices that disrupt the large-scale eddy formation. Lower OASPL and turbulence levels were associated with weakened or diminished large-scale vortical structures. The seemingly similar streamwise vortices generated by these two approaches appear to have markedly different effects on the initial jet structure and the far-field noise spectra. Although Arakeri *et al.* (2003) studied the effect of microjets on the global characteristics of an axisymmetric jet, the small nozzle size limited the capture of the flow field in detail, especially in the cross-plane close to the nozzle exit. Similarly, the fidelity of chevron cross-plane flow-field data has been insufficient to provide a detailed understanding of the streamwise vortex evolution (Opalski, Wernet & Bridges 2005). The present stereoscopic particle image velocimetry (PIV) measurements obtain detailed characteristics of the jet with high enough resolution to determine the nature of the streamwise vortex structure and the associated turbulence fields. The very different flow fields produced by these two devices, coupled with high-fidelity PIV data, provides an opportunity to understand the influence of streamwise vortices on the resulting acoustic fields.

A brief explanation of the measurement set-up and data processing procedure is given in § 2. In § 3.1, the acoustic field characteristics are presented. The streamwise vortex properties are addressed in § 3.2, followed by the jet flow structure with the mean and turbulent shear-layer characteristics in § 3.3.1 and § 3.3.2, respectively. Concluding remarks are presented in § 4.

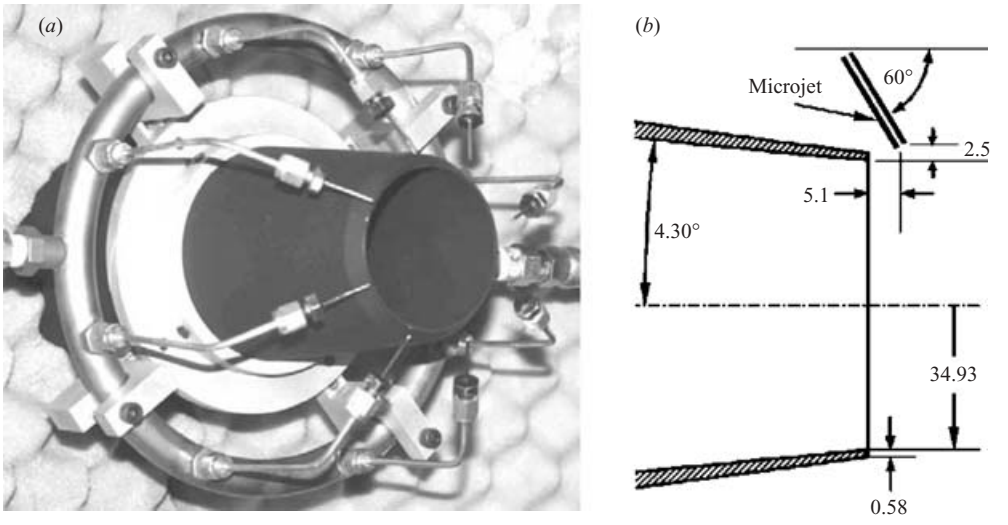

FIGURE 1. The nozzle configuration with microjets (*a*) picture and (*b*) schematic (in mm).

2. Experimental apparatus and procedures

The experiments were conducted in the Quiet Air Facility (QAF) of the Boeing ANP Laboratories located in Seattle, Washington. The QAF is a $9 \times 9 \times 3\,\mathrm{m}^3$ hemi-anechoic test chamber with two muffled air supplies and digitally controlled mass flow rates. Mass flow rates up to $3\,\mathrm{kg\,s}^{-1}$ at 350 kPa pressure can be continuously maintained.

The measurements were carried out at a high subsonic Mach number of 0.9 for three different nozzle configurations, keeping the nozzle pressure ratio (NPR) the same. The base configuration was an axisymmetric converging nozzle with an exit diameter (D) of 69.85 mm. The nozzle was a straight conic section with a 4.30° convergence to mimic typical jet fan nozzle geometries.

The second configuration was the same base nozzle equipped with 8 microjets arranged symmetrically about its periphery and 5 mm downstream (figure 1). Each micro-nozzle was made of a stainless steel tube with a nominal internal diameter of 800 μm. They were positioned at a penetration angle of 60° with respect to the jet flow direction. An optimal air pressure of 700 kPa applied to the microjets was found to minimize the OASPL and used throughout the experiments. At this pressure, the fully expanded Mach number is 2, however, because of the losses in the tubing, it is expected to be around 1.5. Correspondingly, using the isentropic gas relations (NACA 1953), the microjets reach the fully expanded exit velocity of $426\,\mathrm{m\,s}^{-1}$ and density of $1.77\,\mathrm{kg\,m}^{-3}$. The calculated total mass flow rate issuing from all microjets is $\dot{m}_{mj} = 0.007\,\mathrm{kg\,s}^{-1}$, yielding an injected-to-main jet mass flow ratio of $\dot{m}_{mj}/\dot{m}_j = 0.004$. An important parameter determining the penetration of a jet in a crossflow, the momentum flux ratio ($\rho_{mj}u_{mj}^2/\rho_j u_j^2$), is calculated as 2.5.

The third configuration was a chevron type nozzle with 9 equally spaced chevrons around its periphery. The nozzle shown in figure 2 was otherwise identical to the base nozzle with the base of the chevrons located at the baseline nozzle exit plane. The test chevrons are scaled down from a typical full scale primary exhaust chevron. The immersion angle of 13.5° (2.14 mm tip immersion) was larger than that of present state-of-the-art fan chevrons. Consequently, although the resulting flow conditions

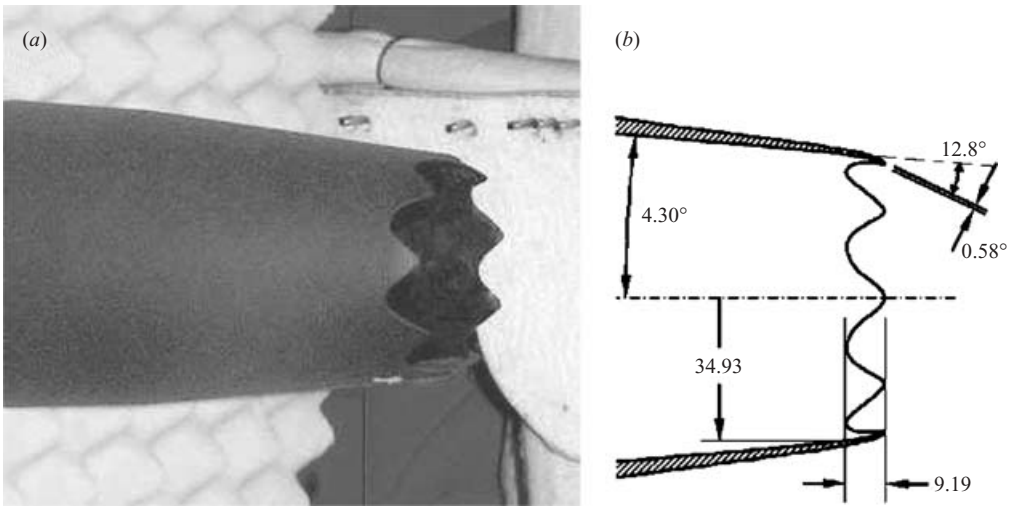

FIGURE 2. The nozzle configuration with chevrons (*a*) picture and (*b*) schematic (in mm).

are not optimum for noise reduction, the higher penetration of the chevrons helped accentuate vortex characteristics in the near-field region of the jet.

For all configurations, the jet stagnation temperature was maintained at 300 ± 3 K. For the present tests, the nominal exit Reynolds number was about 1.3×10^6 (based on exit velocity U_j, and diameter D). With a contraction ratio over 100 and a conical convergent nozzle, Pitot tube measurements at the nozzle exit suggest a laminar velocity profile.

2.1. *Acoustic measurements*

Acoustic measurements were conducted in the anechoic chamber sketched in figure 3. The walls and the floor of the room were covered by polyurethane foam wedges with a low frequency cutoff of about 200 Hz to create a fully anechoic test environment. The acoustic measurements were performed using two linear microphone arrays and a two-dimensional phased array.

The linear arrays were arranged in two lines parallel to the jet axis at distances of $33D$ and $65D$ as shown in figure 3. B&K quarter-inch microphones with an estimated accuracy of ± 0.3 dB were positioned at grazing incidence to the jet axis and located every 5° between 90° and 160°. The second linear array was raised 0.3 m above the first array to reduce acoustic interference. When the first line of microphones are projected to the second line radius at the same angles, they produced OASPL values within ± 0.25 dB.

A nested spiral phased array with 157 microphones (figure 4) was used to measure strengths of acoustic sources in the jet. The phased array consists of a small and a large planar array designed for source resolution in the plane of the jet. The small array is an 81-element multi-arm logarithmic spiral array (Underbrink 2001, 2002), with a diameter of about 0.5 m. The large array is also an 81-element multi-arm logarithmic spiral array, concentric with the small array and having a diameter of about 1 m. The three innermost circles of 9 elements each in the large array are shared with the small array. The small array has a resolution of 2.1 wavelengths for a point source located 0.9 m away on the jet axis. The worst-case side lobes are 11 dB down from 500 Hz to 20 kHz giving a dynamic range of 11 dB. The large-array resolution is 1.0 wavelength with a dynamic range of 11 dB up to 10 kHz. The array's transparency

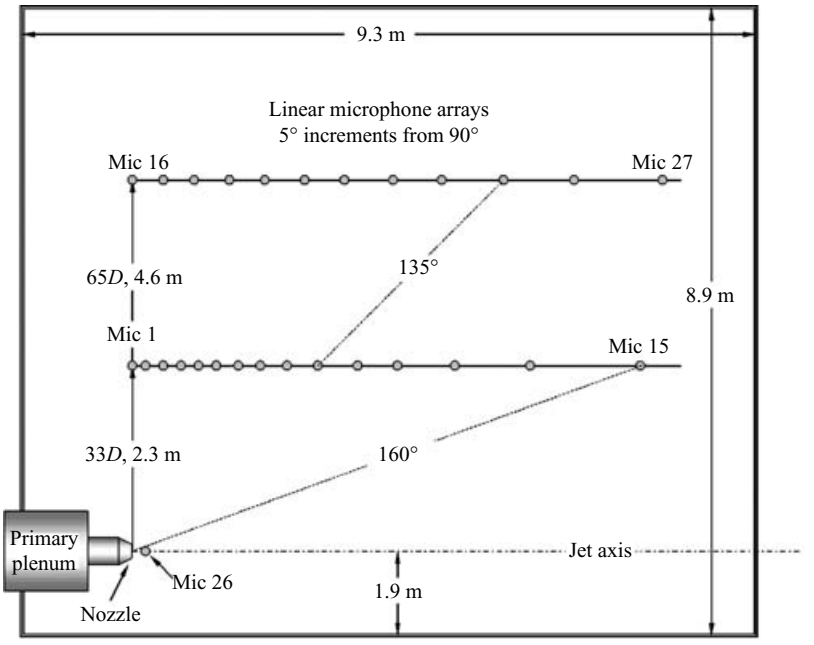

FIGURE 3. Schematic of microphone arrays in the anechoic chamber.

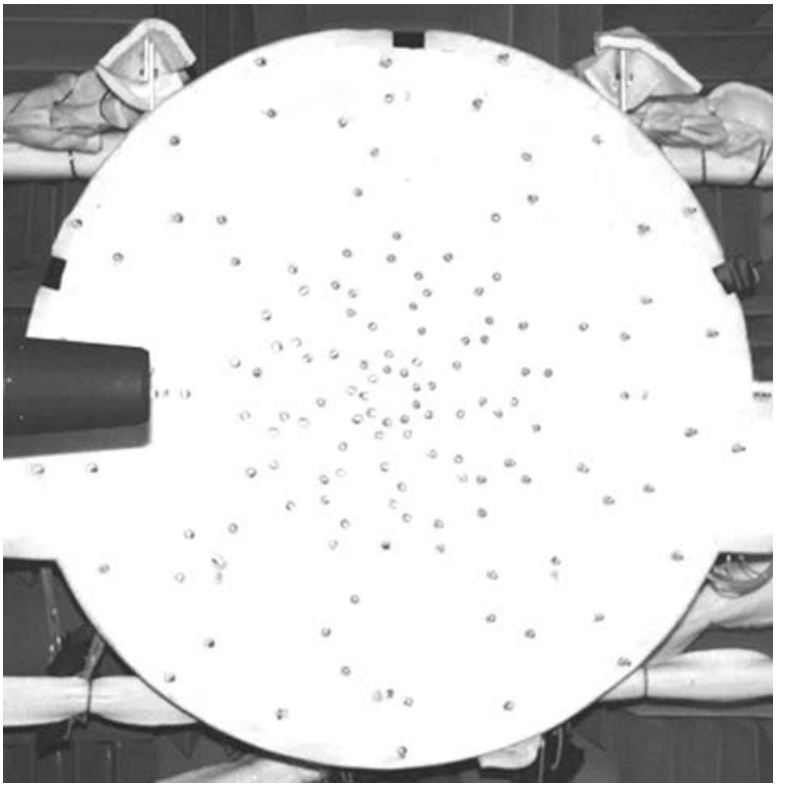

FIGURE 4. Picture of spiral phased array.

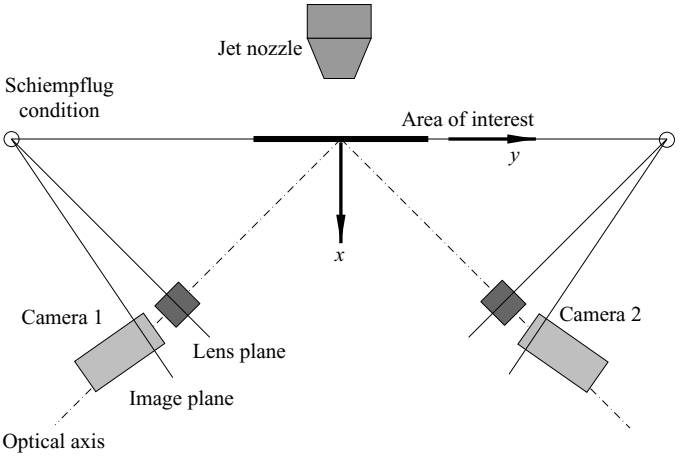

FIGURE 5. Orientation of cameras with Schiempflug condition.

is achieved by mounting the microphones on a low-blockage single-material web, allowing low-frequency sound to pass through the array aperture. Scattering off the structure at higher frequencies above ∼10 kHz is prevented by covering the frame with an effective absorber. The whole array was placed 1 m away from the jet axis with its origin located about 0.3 m downstream of nozzle exit.

2.2. *PIV measurements*

The PIV set-up used in this study was functionally similar to that used in Alkislar *et al.* (2003). In this experiment, a double-pulsed digitally sequenced Nd:YAG laser (New Wave, Gemini II, 140 mJ) was used for illumination. A light sheet of 2 mm thickness was created by suitable combination of spherical and cylindrical lenses. The relatively thick laser sheet facilitates capture of particle images with longer time delays, optimizing measurement accuracy. For this configuration, a time delay of 1.5 μs was used to obtain maximum particle image displacements of ∼5 pixels. The images were recorded by two cross-correlation CCD cameras (sharpVISION^{TM} 1400–DE) arranged in stereoscopic configuration. A 55 mm ($f/1.4$) Nikon macro lens was attached to each camera. The resolution of the cameras was 1360(H) × 1024(V) with pixel size of 4.65 μm × 4.65 μm. When properly synchronized, the camera could acquire 5 image pairs per second in double pulse mode. In the present experiment, the main jet was seeded with submicrometre (∼0.3 μm) oil droplets generated by a modified Wright nebulizer. The ambient QAF air was seeded with smoke particles (∼1–10 μm) produced by a Rosco1400 fog generator.

The cameras were positioned at different angles to the flow field to obtain a stereo view of the laser sheet with orientation shown in figure 5. Each camera image plane was rotated with respect to the lens plane to satisfy the Schiempflug condition for off-axis imaging. This condition is obtained when the measurement plane, lens plane and image plane coincide along a single line, as marked with circles at the intersection of three planes in figure 5. The angle between the optical axes of the two lenses was kept at 90° with each camera having an optimum view angle of 45° to minimize the measurement errors (Alkislar, Lourenco & Krothapalli 2000). Both cameras were calibrated together before the experiments to account for perspective effects. After processing the images from both view angles, the results were combined to give the 3-C velocity field at the laser sheet plane.

Latest versions of the program proVISION^{TM} developed by IDT, were used for the acquisition and processing of the PIV images. The novel algorithm used for the processing of particle images was explained comprehensively in the paper of Lourenco & Krothapalli (2000) and summarized briefly in Alkislar *et al.* (2003). According to this algorithm, and considering all errors inherent in the method owing to practical PIV recording variations, a conservative estimated error of 0.03 pixels was achieved in the displacement measurement. Consequently, with a maximum 5 pixel displacement, a deviation of 0.6 % is expected, corresponding to an error of $\pm 2\,\mathrm{m\,s^{-1}}$ in measured instantaneous velocity. The turbulent quantities obtained from an ensemble of 1200 velocity fields are expected to have an error of 10 % in the most turbulent regions of the shear layer.

Cross-plane measurements were made up to the limit of the traversing mechanism (0.4 m) at 20 axial locations covering the first $5.5D$ of the jet. The measurement locations were clustered close to the nozzle exit in order to capture the rapidly changing flow features with fidelity. At the nozzle exit, the spacing increments started at $0.125D$ and gradually increased to $0.5D$ at the final stations. The data quality was excellent except for very limited regions of the first few stations, where the images were contaminated by reflections from the nozzle exit. It was possible, however, by careful processing to avoid these regions and to gather the complete flow-field information.

2.3. *Postprocessing of raw PIV data*

The traverse mechanism and the laser sheet were aligned with respect to the jet with extreme care. A continuous laser beam was used for the identification of the physical nozzle axis and alignment of the PIV set-up. However, the physical axis of the nozzle does not necessarily coincide with the actual jet axis. There are manufacturing tolerances that can cause misalignment of jet flow. More importantly, the global flow in the anechoic chamber is not fully axisymmetric because of the proximity of the jet to one of the walls of the chamber. In general, the measurement plane has an angle with respect to the cross-plane of the jet because of these influences. Even though the angle mismatch is usually less than 2°, it is important to transform the data obtained from the measurement plane to the actual cross-plane, in order to obtain the correct representation of the vector field and in particular, the derived vorticity field. An explanation of a procedure devised to correctly identify the coordinate system is described in Appendix A.

The processing of the PIV images produces data in Cartesian coordinates. It is natural, however, to use cylindrical coordinates for the representation of circular jets. It is thus necessary to convert the turbulent stress terms to cylindrical coordinates. Instead of calculating the turbulence components from the transformed instantaneous vector fields, the original Cartesian stress components are transformed as described in Appendix B.

3. Results and discussion

3.1. *Acoustic field characteristics*

The acoustic field was investigated using sideline microphones along two parallel lines that were $33D$ and $65D$ away from the jet centreline (see figure 3), and an acoustic phased array (figure 4) that spatially mapped the noise sources in the vertical (X, Z)-plane.

The angular variation of OASPL obtained from the sideline microphone data covering the aft quadrant is given in figure 6 for the three nozzle configurations. Where

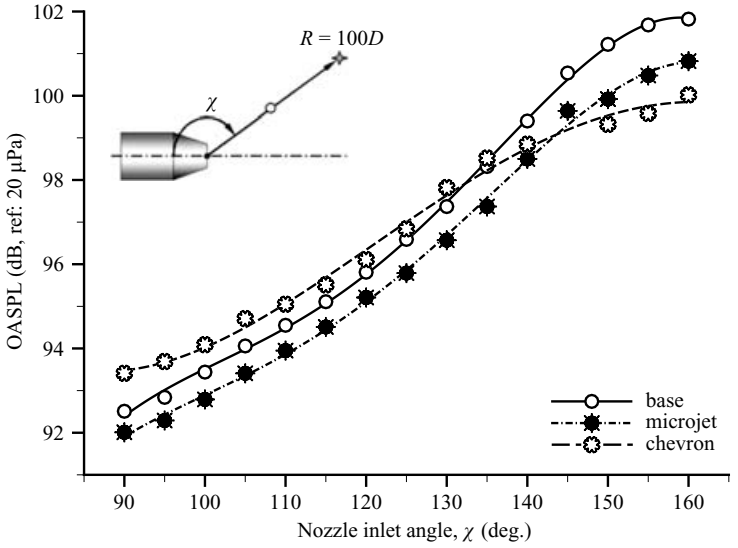

FIGURE 6. OASPL directivity comparison. –○–, base; ☼, microjet; ○, chevron.

available, the data from two microphones located at the same nozzle inlet angle, χ, but at different sideline positions were extrapolated to a distance of $R = 100D$ and then averaged. An excellent match of OASPL was obtained (difference <0.25 dB) between the two sideline microphones for all angles, thus validating the far-field assumption. The directivity curve corresponding to the base case depicts the usual subsonic mixing noise characteristic. It shows a gradual increase to a maximum at an angle of about 160°. For the microjet flow field, the OASPL levels are reduced over the entire range of measurement angles. A reduction of 0.5 dB is observed at 90°, increasing gradually with angle, to 1 dB at the peak radiation angle. The chevron flow produces a remarkably different OASPL distribution. The chevrons increase the noise level at 90° over the base case by about 1 dB. The difference between baseline and chevrons gradually decreases to zero at a cross-over angle of approximately 135°. Beyond this cross-over angle, the noise levels are suppressed, surpassing the performance of microjets beyond 145°. At the peak noise radiation angle of 160°, chevrons achieve a 2 dB reduction.

The narrow band spectra compared in figure 7 at angles of 90° and 160° are representative of the two regions on the directivity curve. In the figure, actual spectra are depicted with smooth lines in order to refine the presentation of the curves. As an example, both the actual spectra and the smooth line are drawn for the chevron case in figure 7(*a*). At both radiation angles, the peak sound pressure level (SPL) for low Strouhal numbers ($St = fD/U_j$) between 0.15 and 0.25 are reduced. The maximum reduction is about 1 dB for the microjets and about 2 dB for the chevrons. However, the noise reduction is observed only up to a cross-over frequency, above which the noise levels increase. The chevrons have a cross-over frequency corresponding to a Strouhal number of 1, whereas the microjet value is more than 3 (the uncertainty of the cross-over value obtained by shifting curves ± 0.3 dB is less then ± 0.1 for chevrons and less than ± 0.4 for microjets at any angle). One of the major differences between the microjet and chevron flows studied here is the change in energy in the high-frequency range of the spectrum.

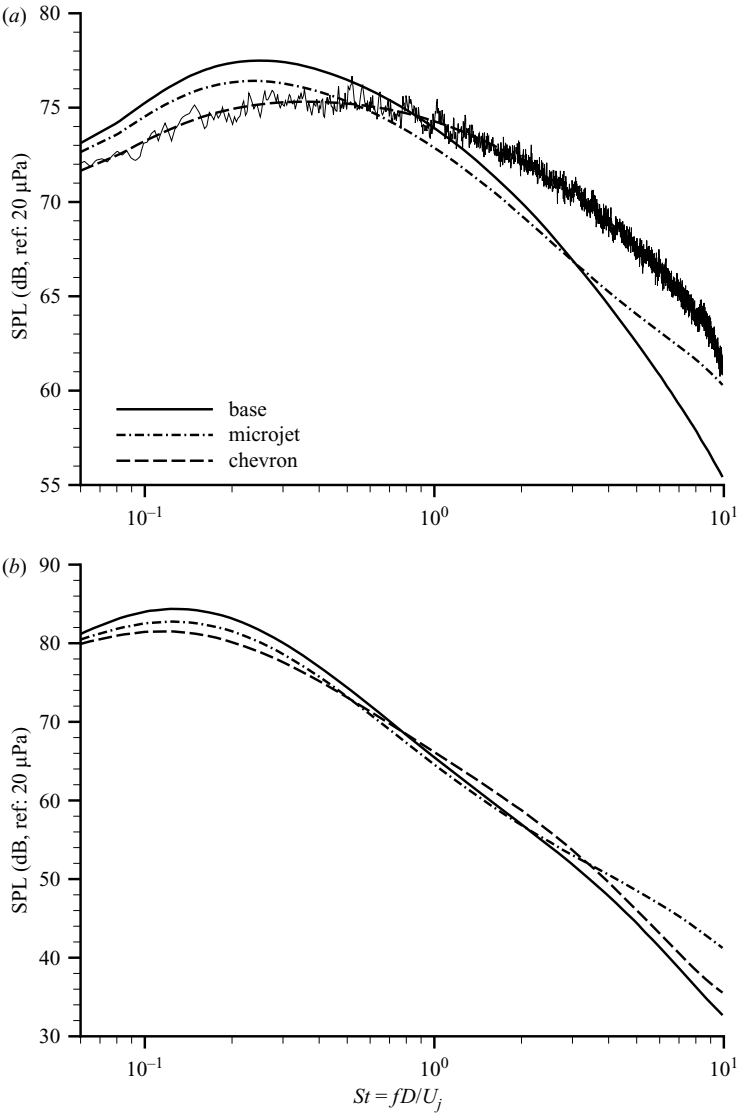

FIGURE 7. The SPL spectra at nozzle inlet angles (*a*) 90° and (*b*) 160°.

At an angle of 160°, the data show that beyond the cross-over frequency ($St > 3$), the microjet noise levels increase beyond those of either the base or the chevrons. The peak frequency observed at the peak radiation angle of 160° corresponds to a Strouhal number of 0.15. This value is close to the universal Strouhal number of 0.2 associated with turbulent mixing noise in compressible jets (Krothapalli, Arakeri & Greska 2004).

In figure 8, the noise source maps obtained from the acoustic phased array are shown for Strouhal numbers of 0.25, 0.5, 1.25 and 2.5, corresponding to source frequencies of 1, 2, 5 and 10 kHz, respectively. The grey level contours represent the base case SPL distribution radiated from the jet as seen by the array. The minimum SPL shown was chosen to be 8 dB down from the maximum to eliminate side-lobe noise. The contour lines corresponding to a constant SPL value allow comparison

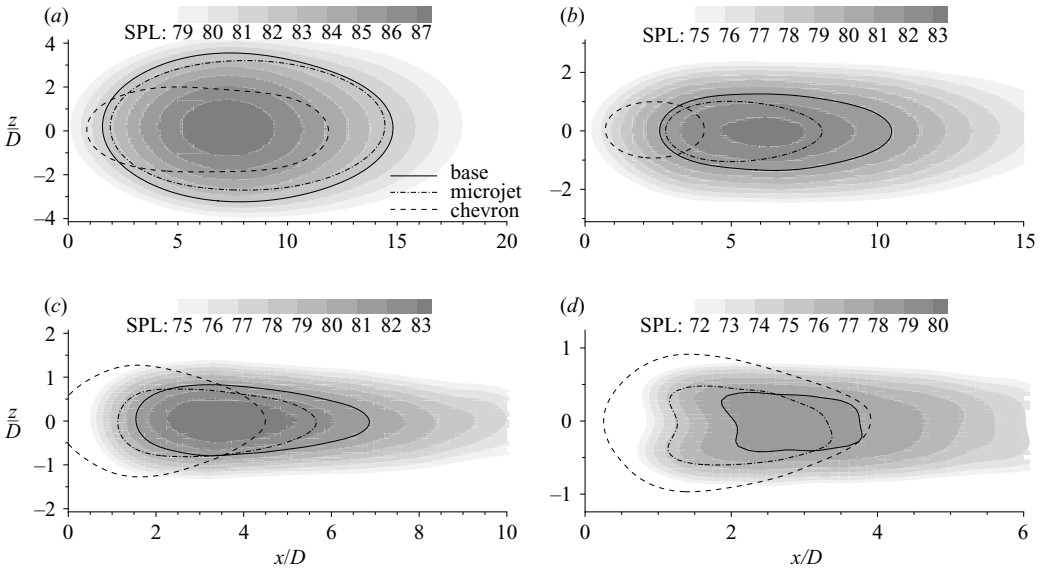

FIGURE 8. Noise maps obtained by acoustic phased array at Strouhal numbers (*a*) 0.25, (*b*) 0.5, (*c*) 1.25 and (*d*) 2.5. The contour lines correspond to a constant SPL level of (*a*) 82 dB, (*b*, *c*) 81 dB, (*d*) 78 dB.

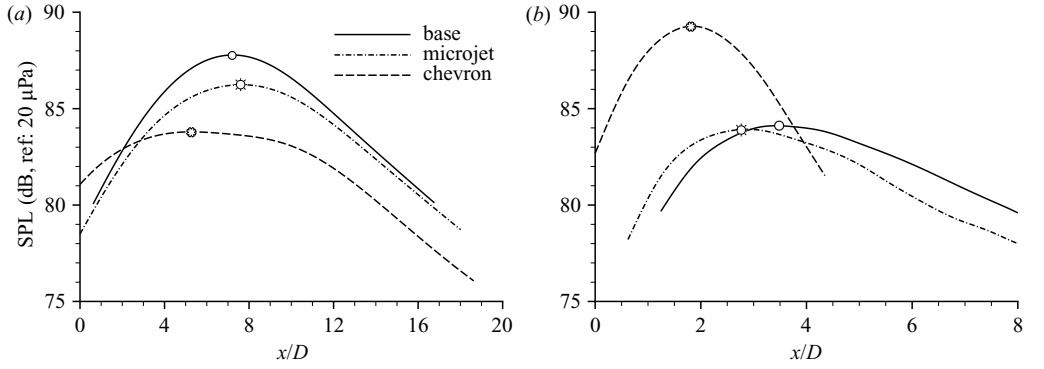

FIGURE 9. Axial variation of source intensities along *x*-axis at Strouhal numbers (*a*) 0.25 and (*b*) 1.25.

of two flow fields. Figure 8(*a*) shows the jet columnar frequency at $St = 0.25$. The sources are distributed over a rather large area, extending $15D$ in the axial direction and $3D$ in the radial direction. Although the contour line for the microjets shows a reduction in the source extent, no discernible change in the location of the $St = 0.25$ sources can be seen. For the chevrons, however, the extent is significantly reduced and the peak source location moves upstream toward the jet exit.

At $St = 0.5$, the reduction in extent obtained by microjets is similar to those of the chevrons with a noticeable upstream shift. For $St > 1.25$, the chevron generated sources occupy a greater area than the base case, originating closer to the nozzle exit. The microjet source area, on the other hand, becomes comparable to the base case. For all cases, the source locations move closer to the nozzle exit as the source frequency increases (note the change in spatial range in figures). Since the eddy size

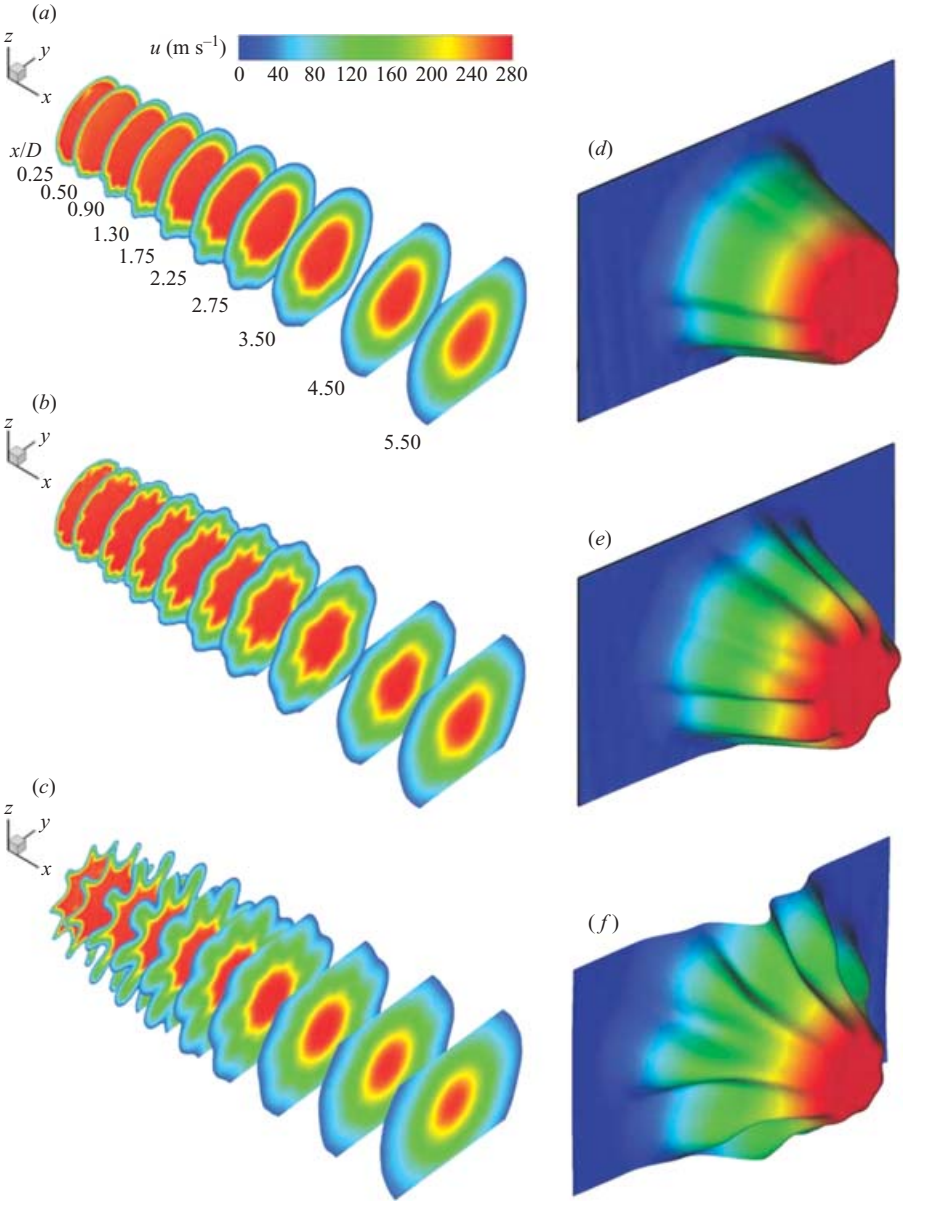

FIGURE 10. The three-dimensional spatial evolution of the jets, (*a*) base, (*b*) microjet, (*c*) chevron, and the velocity profiles at $x/d = 2$, (*d*) base, (*e*) microjet, (*f*) chevron.

scales with the shear-layer thickness, a shift of acoustic energy from low to high frequencies means a shift to smaller flow structures. It also implies that the most intense sources reside in thinner regions of the shear layer. This trend continues at $St = 2.5$, where both microjet and chevron cases reach higher intensities over a larger area than the base case.

The axial variations of source intensities are plotted in figure 9 for Strouhal numbers of 0.25 and 1.25. The lower data cutoff is set to 8 dB relative to maximum SPL value. The peak location is indicated by a single symbol. The results for $St = 0.25$ sources

in figure 9(*a*) show a reduction of 1.5 dB in the peak value for microjets and about 4 dB for chevrons. However, at $St = 1.25$, figure 9(*b*), chevrons increase the peak noise level about 5 dB in contrast to the microjet and baseline. The axial locations where peak values reside also give an insight into the distribution of sources in the flow field. Note that the relevant axial range is much shorter in this figure. At low frequencies corresponding to large-scale structures, the microjet source distribution is very similar to the base case, with lower intensities. A slight movement ($0.5D$–$1D$) of peak noise sources in the downstream direction is discernible which could not be detected in figure 8(*a*). On the other hand, chevrons have more definite influence on the sources. The entire curve moves $2D$ upstream with a much flattened peak. At $St = 1.25$, both methods shift the peak sources upstream. Microjets shift the curve $1D$ upstream without affecting the peak values. In contrast, chevrons greatly foreshorten the profile, shift the peak upstream about $2D$, and increase the peak intensity.

In summary, both microjets and chevrons reduce noise levels below the baseline values in the low-frequency portion of the spectrum. Each exhibits a cross-over frequency at which the SPL increases beyond that of the baseline flow field. This phenomenon is characteristic of tab and chevron devices and known as high-frequency lift. In this respect, the present chevrons produce a greater low-frequency noise reduction and a significantly larger high-frequency lift than the microjets. The observed cross-over frequency is also considerably lower for chevrons. The OASPL values in figure 6 reflect these trends, showing a greater value for the chevrons than the baseline at 90°, crossing over the baseline curve before the peak emission angle has been reached. As reflected by the sideline SPL data, this increase in OASPL derives from the chevron's high-frequency lift. Microjet injection, on the other hand, reduces the OASPL values at all angles, but exceeds the chevron values near the peak emission angle. The noise maps reveal that the extent of the low-frequency sources is reduced for both devices. In contrast, they are increased at high frequencies. In general, the peak source intensities shift upstream, except for the microjet case at low frequencies when a slight downstream shift is observed. Note also that the peak values of the chevron high-frequency sources are significantly higher and further upstream than either the baseline or microjet cases.

3.2. *Streamwise vortex characteristics*

The jet behaviour in the near-field region at each nozzle configuration was investigated through the detailed PIV measurements of the velocity fields. The first $5.5D$ of each jet was examined at 20 cross-sections clustered close to the exit with increasing spacing in the downstream direction. The time-averaged velocity fields and turbulence characteristics were obtained from an ensemble of about 1200 samples at each cross-section.

The spatial evolution of the jets shown in figure 10 describe the mean cross-plane velocity field at several downstream locations. Figures 10(*a*), 10(*b*) and 10(*c*) best capture the three-dimensional features of the evolution of the base, microjet and chevron flows, respectively. The velocity fields are represented by the contours of the axial mean velocity magnitude. The shear-layer outer boundary ($0.1\,U_j$) is defined by a velocity of $28\,\mathrm{m\,s^{-1}}$ as a contour cutoff in the figure. The base case develops axisymmetrically (figure 10*a*), with the exception of a disturbance resulting from a small paint bubble on the nozzle's inner surface. In contrast to the base case, the microjets and chevrons clearly show the different development stages of the jet, particularly in the initial region of the shear layer. In figure 10(*b*), the effect of microjets in the first few measurement planes can be observed from the disturbances made by the injected flow. These disturbances appear as a protuberance at the

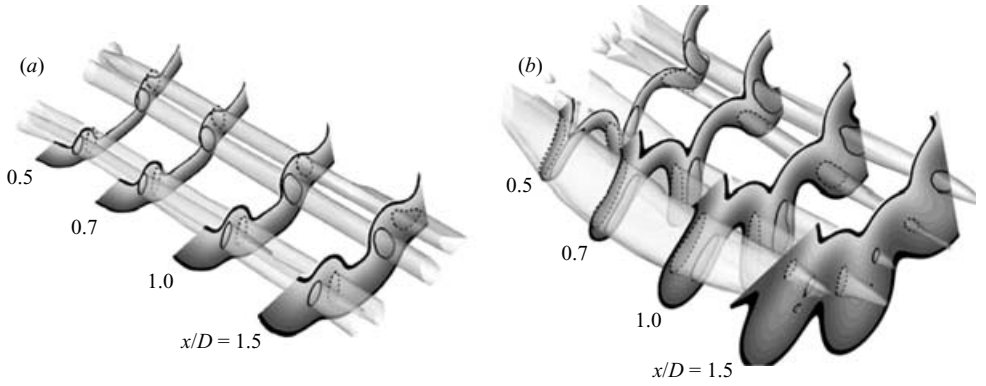

FIGURE 11. Axial vortex development for (*a*) microjets and (*b*) chevrons.

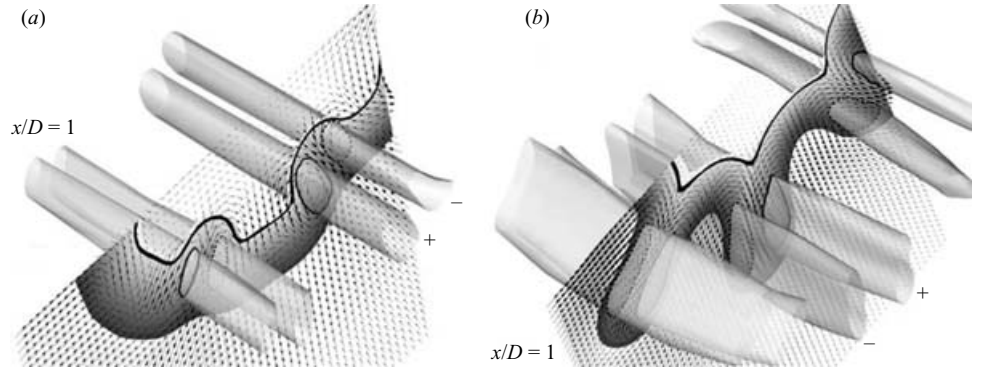

FIGURE 12. Detail at $x/D = 1$ for (*a*) microjets and (*b*) chevrons.

high-speed side of the shear layer. They grow in size with downstream direction and cause the local shear layer to take on a wavy shape. In the chevron flow, the shear layer becomes corrugated right from the nozzle exit with large petals at the low-speed side of the shear layer evident in figure 10(*e*). At $x/D = 5.5$, the effect of the microjets is still visible with minor undulations in the shear layer. In contrast, the initial effect of chevrons vanishes rapidly, and the jet becomes axisymmetric. In addition, the shear layer grows more rapidly than both the baseline and the microjets. The three-dimensional velocity profiles shown in figures 10(*d*), 10(*e*) and 10(*f*) give a better visual representation of each flow field at $x/D = 2$.

The presence of streamwise vorticity is mainly responsible for the changes in the jet structure as seen in figure 10. One of the main advantages of the three-dimensional cross-plane measurements is the determination of streamwise vorticity directly from the in-plane velocity field. The streamwise vortices and their place in the shear-layer development can be described using iso-surfaces of vorticity (figure 11). Contours representing normalized vorticity values of 0.75 and 1.5 are used for microjet and chevron flows. This figure shows two or three isolated vortex pairs within the immediate shear layer. The high- and low-speed boundaries of the shear layer are marked with black contour levels. The intersection of the iso-surfaces with the cross-sections are given by solid and dashed lines for positive and negative values of $\omega_x D/U_j$, respectively. A close-up view at $x/D = 1$ is also presented in figure 12 with the corresponding in-plane velocity field. This view clearly shows the counter-rotating

vortex pairs at each cross-section representing vortex tubes as shown in the figure. The location of the vortex cores within the shear layer also indicates an important physical difference between the two cases. For microjets, it is apparent that the vortex pairs are generated closer to the high-speed side of the shear layer, with the injected fluid penetrating into the main jet. In contrast, the chevrons generate vortices residing more toward the low-speed side of the shear layer with fluid exiting the main jet to the ambient surroundings.

In the microjet case, the vortex pairs are well isolated from each other. The generation mechanism and the structure of these pairs should thus be very similar to that of a jet in a crossflow. However, instead of issuing into the main stream through a boundary layer along a wall, the penetration occurs through the shear layer.

Fric & Roshko (1994) looked at the near-field flow characteristics of a jet in crossflow and identified different types of coherent structures. The coherent structure due to microjet injection is the incipient counter-rotating vortex pair seen in figure 11(*a*), probably the most common one appearing in the far field of the transverse jet. Although there is still no firm consensus on the generation process, many hypotheses exist (see Peterson & Plesniak (2004) for several of them). Several workers (Cortelezzi & Karagozian 2001; Eroglu & Breidenthal 2001; Hasselbrink Jr & Mungal 2001) have simultaneously offered similar explanations: the observed counter-rotating vortex pair is a time-averaged view of unsteady vortex ring interactions of shear-layer vortices (the intrinsically unsteady azimuthal shear-layer vortices shed by the injected jet owing to the Kelvin-Helmholtz instability – note that the scale of these structures is an order of magnitude below the spatial resolution of the present measurement system) in the near-field of the jet. These interactions form intensified vorticity along two streamwise vortex tubes in the time-averaged far field. These explanations are consistent with the experiments and ideas described by Kelso, Lim & Perry (1996) and represented by the vortex tubes of figures 11(*a*) and 12(*a*).

The streamwise vortices generation mechanism seen in the chevron case is different (figures 11*b* and 12*b*). A chevron can be described as a triangular-shaped tab with its apex tilted downstream at some angle to the main stream. Two possible sources of streamwise vortices have been suggested by Bohl & Foss (1999). The first source is the adverse pressure gradient formed upstream of the chevron owing to the angle it makes with the main stream. The second source is vorticity shedding along the trailing edge of the chevron. In the present study, the second source is expected to dominate since the chevrons curve gently into the flow, although their immersion angle is large.

As shown in figure 11(*b*), the vortex tubes originate at the chevron base and pair up with the opposing side of the adjacent chevron (this is the opposite sense of vortex pairing due to a single isolated chevron). Since they form continuously along the edge, the vortex tubes are quite slender and elongated in profile. As evident from the vector field shown in figure 12(*b*), the direction of rotation is opposite to that of the microjets (as indicated on sample vortex pairs from each case). The vortex pairs initially move radially outward owing to their mutually induced velocities until their strength is diminished by entrainment and dissipation.

In figure 13, flow fields of the microjet and chevron cases are compared at axial locations of $x/D = 1$ and 2. The vectors represent the in-plane velocity field; whereas the contour colours represent the streamwise vorticity ω_x normalized by U_j/D. Also shown in the figure are the contour lines of normalized axial mean velocity, u_x/U_j, representing the low-speed boundary of the shear layer, the half velocity line and the high-speed boundary with the values 0.1, 0.5 and 0.9, respectively. The figure shows

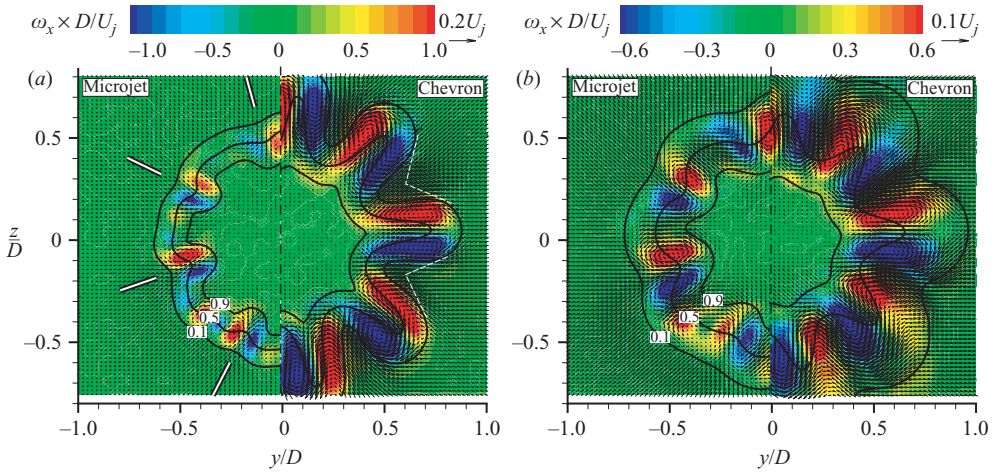

FIGURE 13. Secondary flow comparison at (*a*) $x/D = 1$ and (*b*) $x/D = 2$.

strength and locations of the streamwise vortices in the shear layer. The counter-rotating vortex pairs are clear with red and blue colours representing positive and negative values, respectively. In figure 13(*a*), the difference between the microjet and chevron cases is captured at $x/D = 1$. Also in the figure, illustrated with white lines, are the microjet injectors and chevron tips at their approximate position. At this location, the influence of the microjet injection is in its early stages. There is a large region between the injection points where their effect has not yet been fully felt. At the injection locations, however, strong counter-rotating vortex pairs are created. In comparison, the changes in the shear layer of the chevron flow are strongly affected by the formation of streamwise vortices and commensurate variation in shear-layer thickness. As indicated by the vector field, these vortices transfer low-momentum fluid from the ambient air and induce high-momentum fluid from the jet core into the shear layer. The mass transfer is much stronger for the chevron case, generating radial velocity values in the range $-0.120 < u_r/U_j < 0.136$ compared to the microjet case with values in the range $-0.065 < u_r/U_j < 0.041$. Note that not only are the vortices stronger, but they are also considerably larger.

At downstream location $x/D = 2$ (figure 13*b*), the shear-layers for each case have doubled in thickness and the entire shear layer is influenced by the streamwise vortices. Note that since the in-plane velocity magnitudes are lower, the reference unit vector length has been increased. No significant change is observed in the microjet velocity field with radial velocities in the range $-0.051 < u_r/U_j < 0.055$. On the other hand, in the chevron case, the velocity range is considerably reduced to $-0.071 < u_r/U_j < 0.070$. Note that the maximum inflow occurs in regions between the vortex pairs. Although their magnitudes are similar, the extent of their influence is quite different. For example, the size of the chevron-influence region is of the order of the chevron size itself. Considering the differences in velocity and area of influence, we can conclude that the entrainment due to microjet injection is much less than that of the chevrons.

The maximum average intensity of the axial vorticity at each cross-plane has been calculated from measured velocity data in order to analyse the downstream development of streamwise vortices. The comparison of the microjet and chevron flows is presented in figure 14 for downstream distances where distinct vortices could be identified. As shown by the semi-logarithmic plot, the peak vorticity values decay

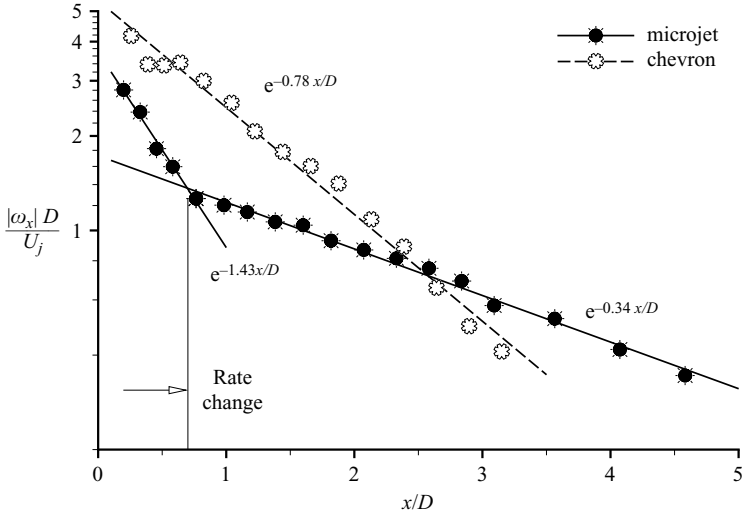

FIGURE 14. Maximum streamwise vorticity variation in the downstream direction.

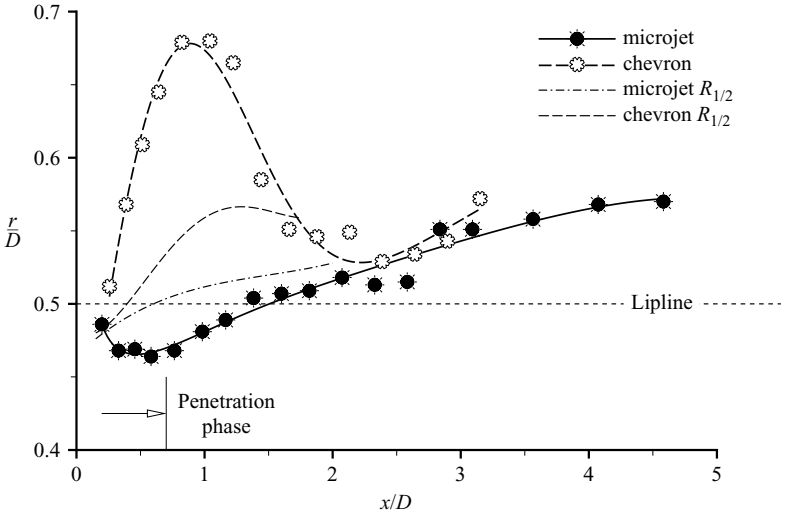

FIGURE 15. Locus of streamwise vortex core.

exponentially. The scatter seen at the first few locations is due to errors in velocity data that are caused by reflections from the nozzle lip. The chevron vorticity field starts with a fairly high $|\omega_x|$ value of 4.2 at the nozzle exit, decays rapidly with an exponential rate of -0.78, and becomes negligible at $\sim 3.25D$. In contrast, the microjet vortices start at a lower $|\omega_x|$ of about 2.8. Although their initial decay rate is greater than the chevron case (exponential rate of -1.43), they switch to a much slower rate of -0.34 after $x/D = 0.7$, and persist up to $4.5D$ before becoming immeasurable. Similar exponential decay rates have been reported in literature for counter-rotating vortices generated by jets in low-velocity crossflows (Johari & Rixon 2003).

In figure 15, the radial location of the vortex core (maximum vorticity) is compared for both cases as a function of x/D. Also drawn in the figure up to about $x/D = 2$ are the loci of the half-velocity radius $R_{1/2}$ obtained from the profiles at the azimuthal

angles at which the vortex cores reside. Here, $R_{1/2}$ is the half-velocity radius (radial location where the axial velocity is half of the local centreline velocity, $u = 0.5\ U_j$). The microjet data indicate that their penetration causes vortices to be generated in the high-speed side of the shear layer. They continue to penetrate into the jet for $x/D < 0.7$, after which they move radially outward in the shear layer. This is exactly the same region where the decay in vorticity switches from a higher rate. In contrast, the chevron vortices appear to remain on the low-speed side of the shear layer for $x/D < 2$, after which their strength rapidly diminishes.

In summary, microjets and chevrons both produce axial vorticity over and above the baseline values. For $x/D < 2$, the microjet and chevron vortex core locations are on the high- and low-speed sides, respectively, but appear to approach a common $R_{1/2}$ line. The microjet and chevron axial vortex pairs rotate in the opposite (figure 12). The increases in strength are significant in the near-field region of the jet, with chevrons producing greater peak values. The exponential decay rate of the peak vortex strength has an abrupt switch to a lower rate for the microjets at $x/D = 0.7$ where the penetration to the main stream is completed. On the other hand, the chevron vortices decay at a constant, but higher rate. The difference in decay rates results in more persistent microjet vortices remaining in the flow much longer as compared to chevron vortices.

3.3. *Jet flow characteristics*

The different core loci and decay rates are important distinctions between the two vortex generating methods and lead to differences in shear-layer structure. Consequently, the changes in the jet mean and turbulence characteristics occur, resulting in different acoustic properties. A detailed analysis of the jet flow in the presence of axial vortices is presented here.

3.3.1. *Mean characteristics*

The variation of the axial mean velocity along the centreline normalized by the exit velocity is shown in figure 16. As the figure illustrates, the measurement locations are all within the potential core, since no significant decay in the centreline velocity can be observed. The scatter in the initial locations of the base case are due to fluctuations in the tunnel operating conditions.

In order to describe the development of the shear layers, a shear-layer thickness δ, is defined as the distance between the radial locations at $u/U_j = 0.1$ and 0.9. However, this thickness varies greatly in the azimuthal direction owing to the chevron petals and microjet injection. This is particularly true for the chevron case as seen in figure 10(*c*). Accordingly, δ_{max} and δ_{min} are obtained as functions of x/D for azimuthal angles where the maximum and minimum thicknesses are observed. The average is then taken as the shear-layer thickness δ, at that x/D and compared with other cases. In figure 17, the development of the shear-layer thickness in the downstream direction is shown for the jet with chevrons. Axial velocity contours at $x/D = 1$ are also shown to illustrate the azimuthal angles used for the computation of δ_{max} and δ_{min}. The minima in shear layer thickness are observed at the chevron tip locations with maxima occurring at mid-angles between the tips. The dramatic difference between δ_{max} and δ_{min} is evident in the first 3 diameters of the jet flow. δ_{max} grows rapidly from the beginning and at $x/D = 1$, it approaches nearly three times δ_{min}. Chevrons stretch the shear layer such that as much as a 15 % reduction in δ_{min} with respect to the base case is measured in the first $1.25D$. As a consequence of the thin shear layer, azimuthal vorticity and turbulence components increase in these regions, as

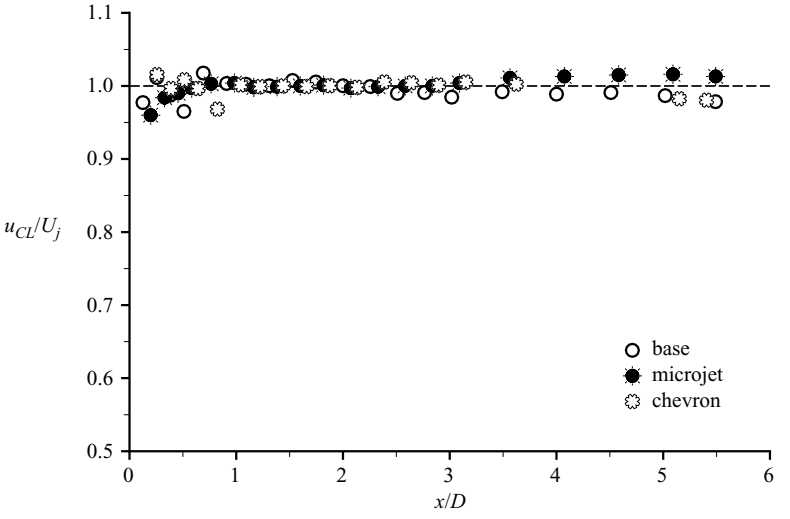

FIGURE 16. Centreline velocity distribution.

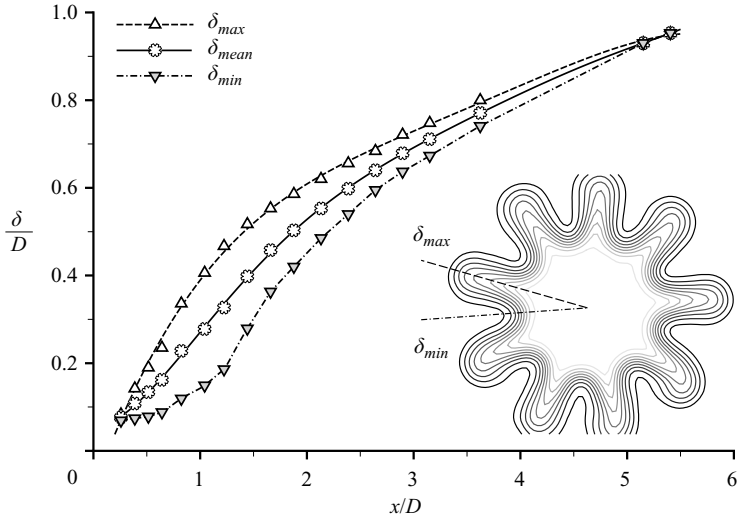

FIGURE 17. Shear-layer thickness development for chevrons.

shown in §3.3.2. For the microjet case, the maxima occur at the locations of microjet penetration, and the minima occur between the injection points (see figures 10*b* and 13*a*). Accordingly, δ_{min} observed for the microjet are nearly identical to the base case.

The variation of δ/D with x/D in the axial direction is compared for all the cases in figure 18. The first observation is the great difference in the initial growth rate of the chevron shear layer up to $x/D = 2.5$. This is evidence of the increase in entrainment owing to the large affected area between vortex pairs and the rotation direction (high speed to low speed). For $x/d > 2.5$, the shear-layer growth rate relaxes to a value similar to the base case. The microjet results are consistent with the previous studies (Arakeri *et al.* 2003; Krothapalli *et al.* 2003, 2004; Alkislar *et al.* 2005). In these studies, it was shown that the shear-layer thickness initially increases slightly within a few diameters of the exit. The growth rate usually decreases after 3 diameters

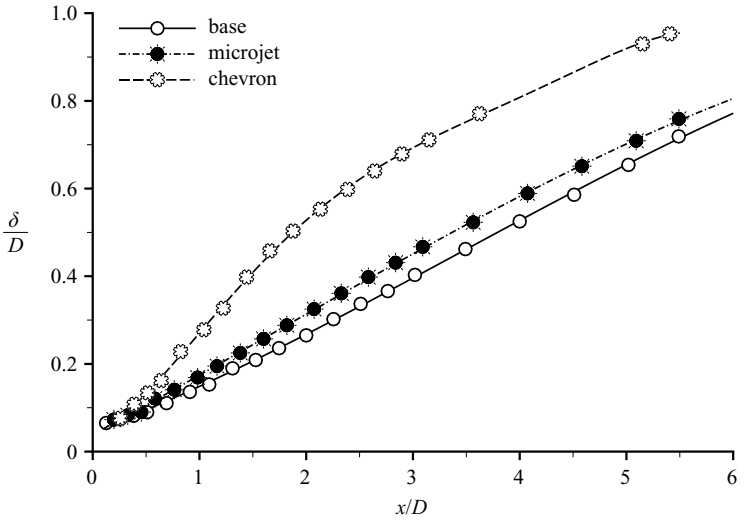

FIGURE 18. Shear-layer development for all cases.

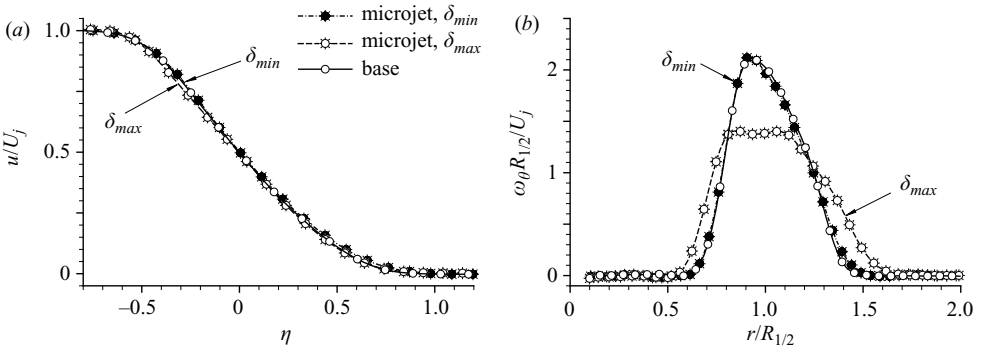

FIGURE 19. Comparison of (*a*) velocity and (*b*) vorticity profiles at $x/D = 2$ for the microjets.

downstream of the exit, increasing the potential core length and reducing the jet spreading. In the present study, growth rates at $x/D = 3.5$ for the base, microjet, and chevron cases are 0.13, 0.12 and 0.10, respectively.

As evident from figure 10, the velocity profiles change dramatically in the azimuthal direction because of the presence of streamwise vortices. The development of velocity profiles was investigated in detail at angles where the shear layer obtains δ_{min} and δ_{max}. Axial velocity and azimuthal vorticity profiles for the baseline, microjet and chevron flow fields are presented in figures 19, 20 and 21. In figure 19(*a*), the normalized velocity profile for the microjet case at an axial location of $x/D = 2$ is compared to that of the baseline jet. The axial velocity u is normalized by U_j, with $\eta = (r - R_{1/2})/\delta$ used as the radial parameter. At this location, the mean velocity profile shows self-similarity, matching the similarity profiles of Arakeri *et al.* (2003). Although the three-dimensional flow seems uninfluenced by the induced velocity field of counter-rotating vortices, a slight divergence from the baseline axial velocity profile can be seen for the microjet's δ_{max} profile. The δ_{min} profile is essentially identical to that of the base case.

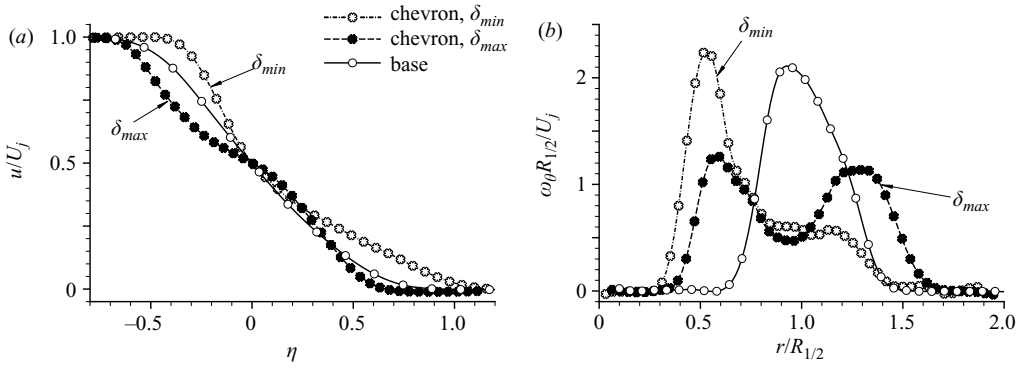

FIGURE 20. Comparison of (*a*) velocity and (*b*) vorticity profiles at $x/D = 2$ for the chevrons.

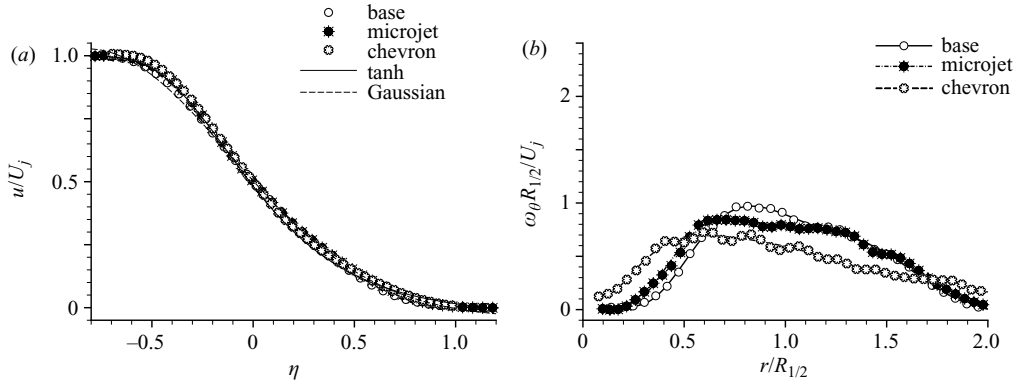

FIGURE 21. Comparison of (*a*) velocity and (*b*) vorticity profiles at $x/D = 5$.

Another important parameter for shear-layer stability is the azimuthal vorticity, ω_θ. The comparison of vorticity profiles between the baseline and microjet flows at $x/D = 2$ is shown in figure 19(*b*). The vorticity is scaled by $R_{1/2}$ and jet exit velocity U_j, and the radial distance r by $R_{1/2}$. The baseline vorticity profile agrees well with the results of Arakeri *et al.* (2003). The δ_{min} curve shows no significant variation from the base case, indicating that the influence of the microjets is not yet felt between the penetration points. In contrast, for δ_{max} (e.g. where penetration occurs) the peak vorticity is reduced by 35 %, indicating a more stable velocity profile.

The chevron velocity and vorticity profiles are compared with the baseline case in figure 20. In contrast to the microjet case, the influence of the strong streamwise vortices is evident from the change in axial velocity profiles shown in figure 20(*a*). The chevron's δ_{max} velocity profile contains three inflection points, indicating a high degree of instability. The vorticity profiles also demonstrate radical changes. The δ_{min} curve shows that the peak azimuthal vorticity ω_θ moves further into the high-speed side of the shear layer with a value about 7 % higher than the base case. On the other hand, the δ_{max} data clearly illustrate three local extrema corresponding to the three inflection points in the velocity profile. The lower value of peak vorticity, ω_θ, can be attributed to the thick shear layer, which is twice as thick as the baseline at this axial location. The location of the peak is again located in the high-speed side of the shear layer.

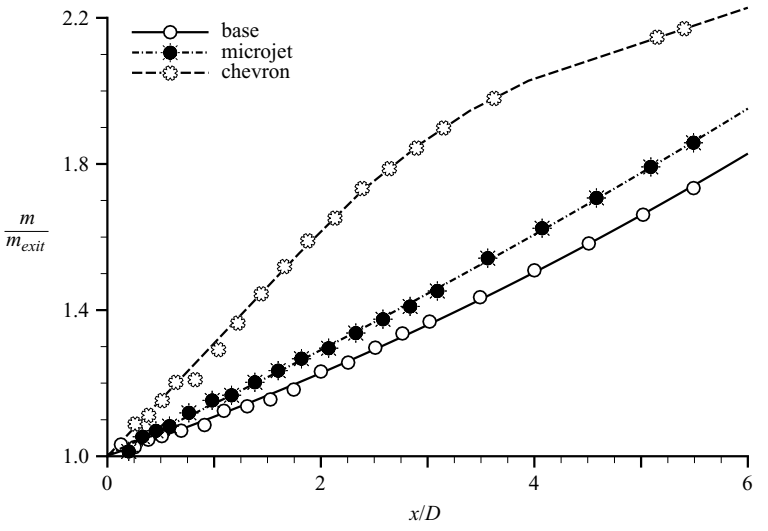

FIGURE 22. Axial variation of total mass flow rate.

At $x/D = 5$, the velocity profiles of the three cases approach a similarity profile (figure 21*a*). The comparison between the azimuthal vorticity profiles of all cases is shown in figure 21(*b*). At this location, all profiles tend toward the baseline shape as the jets ultimately become axisymmetric. For this reason, no distinction can be made between δ_{max} and δ_{min}. The lower peak vorticity values produced by the microjets and chevrons result from the increase in the shear-layer thickness (figure 18).

The variation of axial mass flow rate with x/D, $\dot{m} = \int\int \rho\, u\, \mathrm{d}y\, \mathrm{d}z$, normalized by the exit mass flow rate is given in figure 22. For these calculations, isentropic relations incorporating the velocity and the core total temperature are used to approximate the value of local density in the shear layer. The nearly linear curves of the baseline and microjet cases show 6 % larger mass flow rates for microjets. The chevrons show a dramatic increase for $x/D < 3$ where mass flow rates 40 % higher than the base case are observed. Beyond $x/D = 3$, the entrainment rate of the chevrons decreases below that of the base and microjets. This directly indicates that most of the mixing due to chevron-generated streamwise vortices occurs in the first $2D$ of the jet flow, increasing the entrainment. These findings are consistent with the shear-layer growth rates described in previous paragraphs and turbulence characteristics that will be discussed in the next section.

3.3.2. *Turbulence characteristics*

In addition to affecting the mean characteristics of the shear layer, streamwise vortices change the development and distribution of turbulent quantities. The jet's mixing rate, generation of shear stresses, and ultimately, the production and dissipation of turbulent kinetic energy are all related. In this discussion, the $x/D = 2$ cross-section data (figure 23*a*) are used to examine the general three-dimensional trends. A half-plane comparison at this particular axial location is made between the cases, since the turbulence levels are of the same order and exhibit a high degree of symmetry.

In figure 23(*a*), axial turbulence intensity, u'_x/U_j, is compared for the microjet and chevron cases. The baseline cross-section data is not shown because of its axisymmetric character. As was done previously, contour lines of u_x/U_j, represent

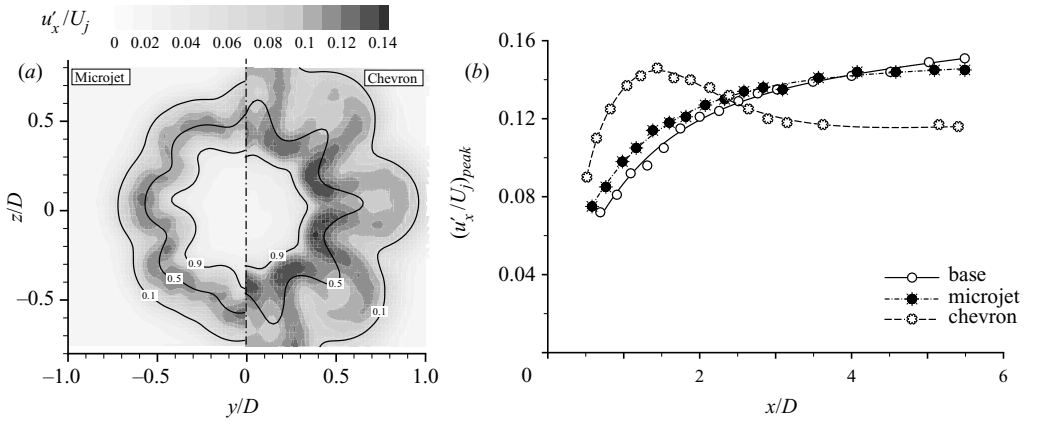

FIGURE 23. Axial turbulence intensity, u'_x/U_j (*a*) at $x/D = 2$, (*b*) peak value variation in the downstream direction.

the low-speed, the half-velocity line and the high-speed boundary of the shear layer with $u_x/U_j = 0.1$, 0.5 and 0.9, respectively. These lines clearly identify the shear-layer boundaries and the distribution of the quantities of interest. As seen in this figure, the chevrons generate higher turbulence values and encompass a much larger area than the microjets. Microjets, on the other hand, produce a stabilizing effect that can be seen by the reduced turbulence levels at azimuthal angles corresponding to the δ_{min} (penetration angle). In the shear layer, the maximum levels are positioned radially along the half-velocity contour on the low-speed side (note that, although not shown here, the peak values for $x/D \leqslant 1$ occur at the injection angles, about the half-velocity line). For the chevron case, on the other hand, the turbulence levels are higher in magnitude with maximum values observed in the high-speed side of the shear layer at an azimuthal angle corresponding to δ_{max}.

In figure 23(*b*), the variation of peak u'_x/U_j value with axial distance is compared for all three cases. The chevron turbulence levels increase rapidly to a maximum value of 0.145 at an axial distance of $1.5D$, and then decrease gradually to a nearly constant value of 0.12 at $x/D = 3$. The microjet case follows a variation similar to the base case, increasing monotonically with declining rate to a value of about 0.15 at the end of the measurement range. Although the turbulence levels for the microjet case are initially higher than for the base case, they gradually relax to the baseline level and then remain below it for $x/D \geqslant 4$.

In a fashion similar to the presentation of velocity and vorticity profiles, the turbulence intensity can be examined in detail with radial profiles taken at δ_{min} and δ_{max}. The microjet profiles in figure 24 are similar to the base case, showing somewhat increased turbulence levels. In contrast, the chevron profiles in figure 24(*b*) are greatly different. At this axial location, the turbulence profiles resemble the curves of azimuthal vorticity (see figure 20*b*). Since $\eta = 0$ corresponds to the half-velocity position in the shear layer, it is obvious that the increased axial turbulence levels are located on the high-speed side of the shear layer. This suggests a correlation between the axial vorticity and increased turbulence intensity for both the microjets and the chevrons.

The next quantity of interest is the radial turbulence intensity u'_r/U_j. Its distribution in the $x/D = 2$ cross-plane is shown for microjets and chevrons in figure 25(*a*). The figure shows that, u'_r/U_j for the microjet case is similar to u'_x/U_j in figure 23(*a*),

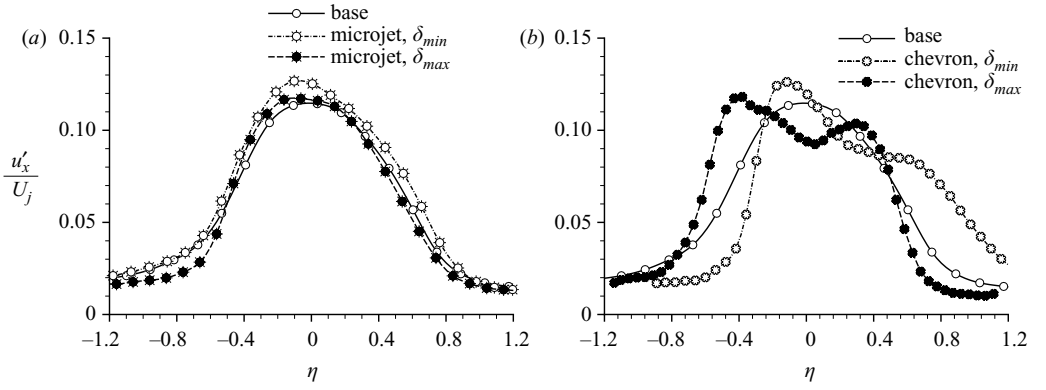

FIGURE 24. Axial turbulence intensity, u'_x/U_j profiles at $x/D = 2$ for (*a*) microjets and (*b*) chevrons.

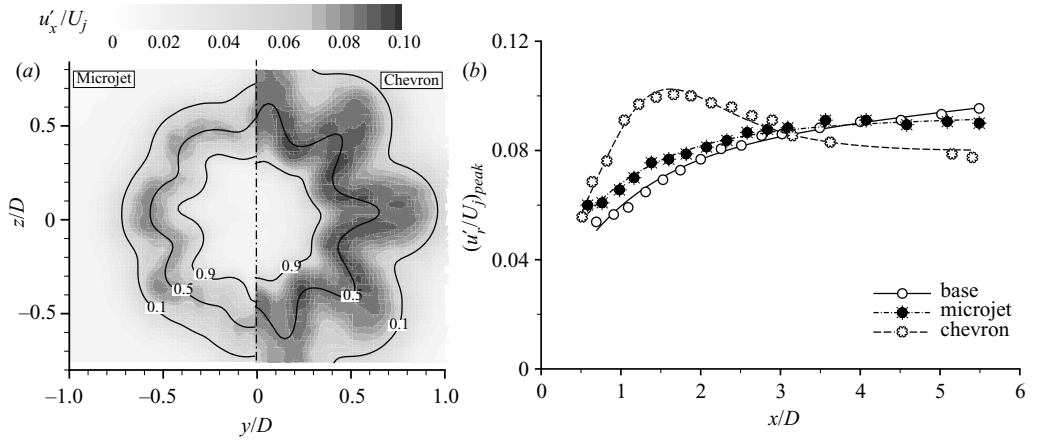

FIGURE 25. Radial turbulence intensity, u'_r/U_j at $x/D = 2$, (*a*) at cross-section $x/D = 2$, (*b*) peak-value variation in the downstream direction.

except with reduced fluctuation levels. The decrease at injection locations is again evident. The radial turbulence intensity in the chevron case, on the other hand, covers a broader region along the half-velocity line ($R_{1/2}$) with a more grdual azimuthal variation. The maximum values are reached at azimuthal angles corresponding to δ_{min}. The peak values of u'_r/U_j are compared in figure 25(*b*) as a function of x/D. The trends are very similar to u'_x/U_j. For the chevron case, a local peak is observed for each normal component of stress at $x/D = 1.5$. A maximum value of 0.100 is reached for the chevron's radial component. The curves of u'_r/U_j for the microjet and base cases, on the other hand, monotonically increase to the values of 0.090 and 0.095, respectively. The peak radial turbulence for the microjet case becomes almost constant after $x/D = 4$. The radial profiles of this quantity show the same behaviour as u'_x/U_j, but with a broader and more gradual rate of change.

The azimuthal turbulence intensity, u'_θ/U_j, is shown in figure 26. The data in figure 26(*a*) demonstrate the same characteristics for the microjets as u'_x/U_j and u'_r/U_j at $x/D = 2$. However, the distribution of u'_θ/U_j differs within the shear layer. For this quantity, the highest values occur on the high-speed side of the shear layer at angles corresponding to δ_{max}, rather than to δ_{min}. In addition, the peak values are

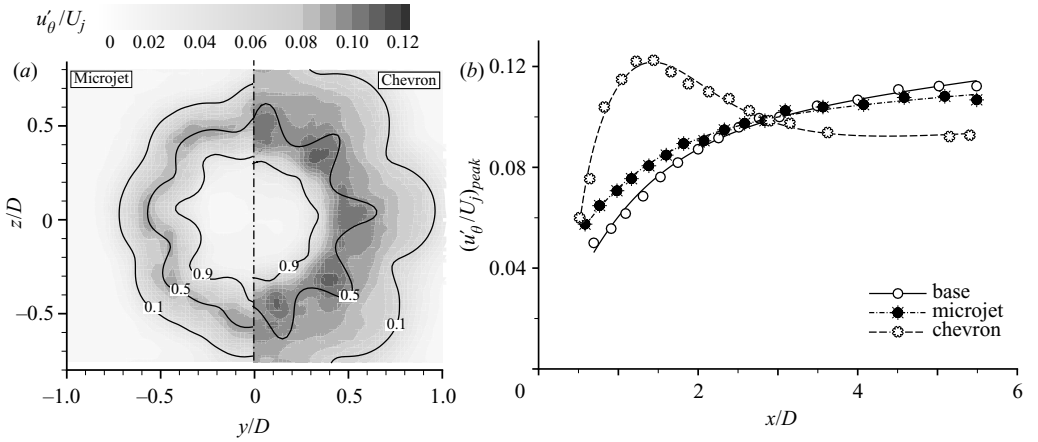

FIGURE 26. Azimuthal turbulence intensity, u'_θ/U_j (*a*) at cross-section $x/D = 2$, (*b*) peak-value variation in the downstream direction.

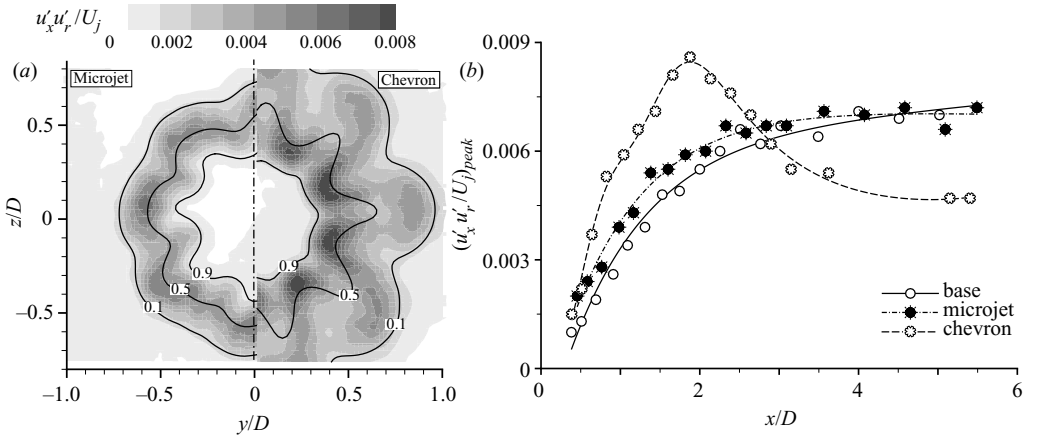

FIGURE 27. Transverse turbulence stress, $\overline{u'_x u'_r}/U_j^2$ (*a*) at cross-section $x/D = 2$, (*b*) peak-value variation in the downstream direction.

lower than u'_x/U_j, but greater than u'_r/U_j. The axial variation of the peak values are plotted in figure 26(*b*). Considering the chevron case, the local maximum is once again observed at a downstream location of $x/D = 1.5$ with a value of 0.122. Microjets and chevrons obtain values of 0.107 and 0.122, respectively. Similarly to u'_r/U_j, the peak values for the microjets become nearly constant downstream for $x/D \geqslant 4$.

Note that u'_θ/U_j and u'_r/U_j are quite different at a given axial location showing the highly anisotropic nature of the flow field. The peak values for each component are also observed at different regions of the shear layer.

Another important parameter is the transverse turbulent shear stress, $\overline{u'_x u'_r}/U_j^2$. The distribution of normalized values at $x/D = 2$ are compared in figure 27(*a*) for the microjet and chevron cases. The first observation is that both follow the u'_x/U_j distribution shown in figure 23(*a*), although with sharper peaks. For both cases, the peak values are located at δ_{min}. Similar to the trends of previous turbulence parameters, the maximum values of $\overline{u'_x u'_r}/U_j^2$ values are located on the low-speed side of the shear layer for the microjet and on the high-speed side for the chevrons. An

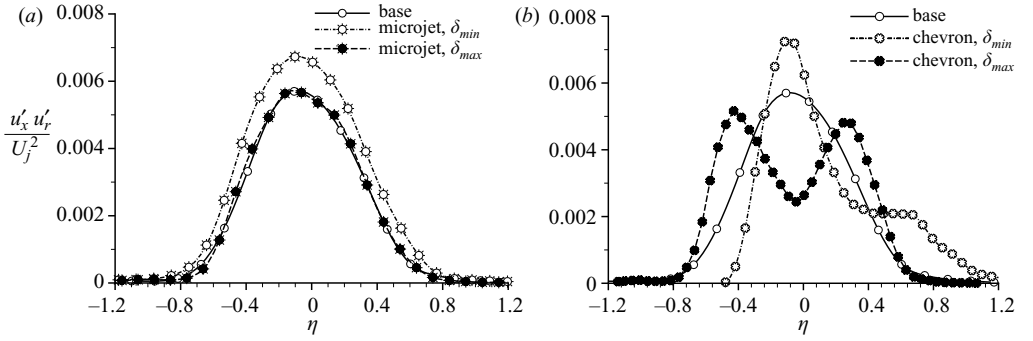

FIGURE 28. Transverse turbulence stress, $\overline{u'_x u'_r}/U_j^2$ profiles at $x/D = 2$ for (*a*) microjets and (*b*) chevrons.

additional difference is that for the microjets, this region is in an area of outward radial velocity (high energy to low energy), whereas for the chevron case it is in a region of inward radial velocity.

In figure 27(*b*) the axial variation of peak $\overline{u'_x u'_r}/U_j^2$ values are compared for the three cases. The chevron case reaches its local maximum of 0.0086 at $x/D = 1.75$ and falls to 0.0047 at $x/D = 5$, which is lower than the other two cases. This is consistent with the chevron's increased shear-layer growth rate in the first $2D$ (figure 18). For the microjet and base cases, the stress increases monotonically from the exit with values of 0.002 and 0.001 to the peak value of 0.0072. The values measured in the present experiments are in general agreement with the values given in Arakeri *et al.* (2003).

The transverse profiles of $\overline{u'_x u'_r}/U_j^2$ obtained at $x/D = 2$ are compared in figure 28. In figure 28(*a*), the microjet's profile shape is similar to the base case. It has a larger turbulence level at δ_{min}, and virtually replicates the δ_{max} values. When compared to the baseline, on the other hand, the chevron profiles at both δ_{min} and δ_{max} are dramatically different (figure 28*b*). At δ_{min}, the chevrons achieve a higher, but narrower peak, with a low plateau extending into the low-speed side of the layer. The saddle-shape stress profile at δ_{max} exhibits distinct peaks in both the high-speed and low-speed side. Moreover, the peak on the high-speed side located at $\eta = -0.5$ reaches axial velocities of $u_x = 0.85\, U_j$. These profiles are in excellent agreement with the azimuthal vorticity profiles (see figure 20*b* noting different radial normalization) which are, in turn, directly related to the transverse turbulent shear stresses.

Other quantities obtained from the measurements are the remaining turbulent shear stresses represented with $\overline{u'_x u'_\theta}/U_j^2$ and $\overline{u'_r u'_\theta}/U_j^2$. Their cross-plane distributions are compared in figure 29 for the sake of completeness. The intimate relationship between these quantities and the streamwise vortices is evident from the peak locations in the flow cross-section. At the angles corresponding to δ_{min} and δ_{max}, the values of these components approach zero owing to nearly constant mean azimuthal velocity, u_θ.

Finally, the distribution of normalized total turbulent kinetic energy, q^2/U_j^2, calculated from the measured three normal components of turbulence ($q^2 = (u'^2_x + u'^2_r + u'^2_\theta)/2$) are given in figure 30(*a*). The distribution characteristics are similar to u'_x/U_j, since it is the dominant component in the shear layer. The comparison of streamwise peak values is given in figure 30(*b*). The peak of the chevron curve is $\sim x/D = 2$ with a value of 0.0194. Chevron values of q^2/U_j^2 decrease to an almost constant value of 0.0145 for $x/D > 3.5$. At the end of the measurement region, the microjet case reaches

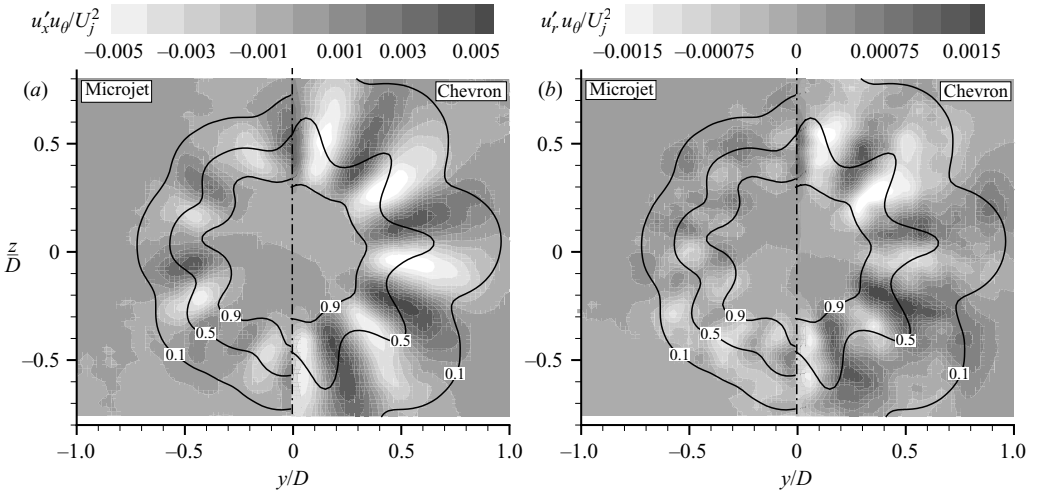

FIGURE 29. Transverse turbulence shear stresses at $x/D = 2$, (*a*) $\overline{u'_x u'_\theta}/U_j^2$ and (*b*) $\overline{u'_r u'_\theta}/U_j^2$.

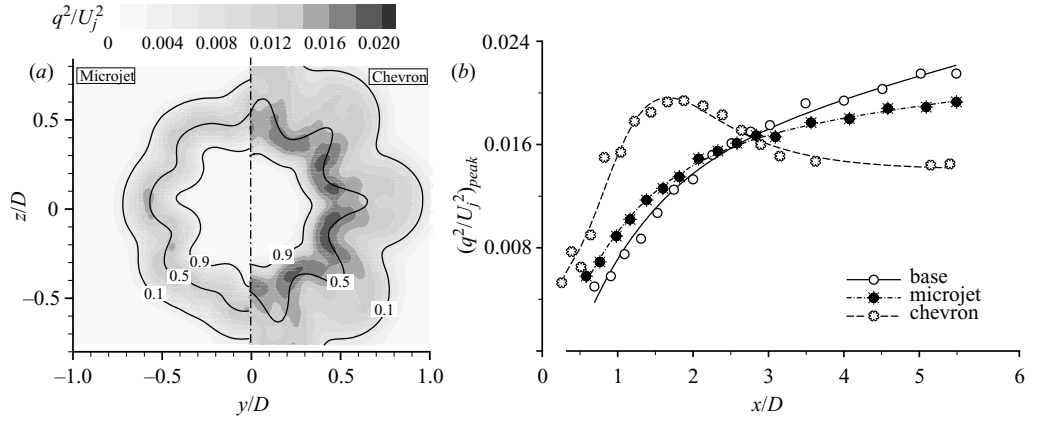

FIGURE 30. Turbulent kinetic energy, q^2/U_j^2 (*a*) at cross-section $x/D = 2$, (*b*) peak value variation in the downstream direction.

a value of 0.0193, 10 % lower than the base case (0.0215). The chevrons, on the other hand, achieve a reduction of about 30 %. The axial variation in q^2/U_j^2 shows the dramatic suppressive effect of these devices for $x/D > 3$. These lower values indicate the rapid dissipation of upstream turbulent energy and lower production owing to decreased shear in the thicker shear layer. The growth of large-scale structures may be inhibited because of azimuthal interference of streamwise vortices and large dissipation by fine-scale mixing occurring for $x/D < 3$.

As for the mean flow, the distribution of turbulence quantities for each case becomes nearly axisymmetric for $x/D > 5$. Since there is little or no variation with angle, radial profiles at this location are sufficient to describe the flow field. The axial turbulence intensity and transverse turbulent stresses are compared for all cases in figure 31 at $x/D = 5$. Once again, the results of both quantities show that the microjet and base cases are almost identical at this axial location. On the other hand, as expected from

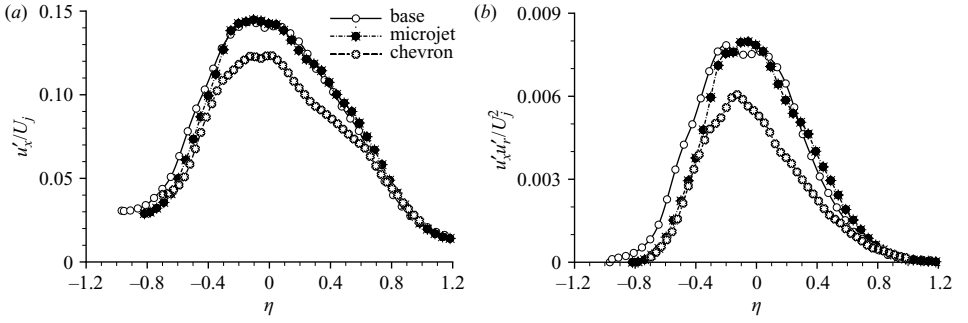

FIGURE 31. Comparison of turbulence profiles at $x/D = 5$, (*a*) u'_x/U_j, (*b*) $\overline{u'_x u'_r}/U_j^2$.

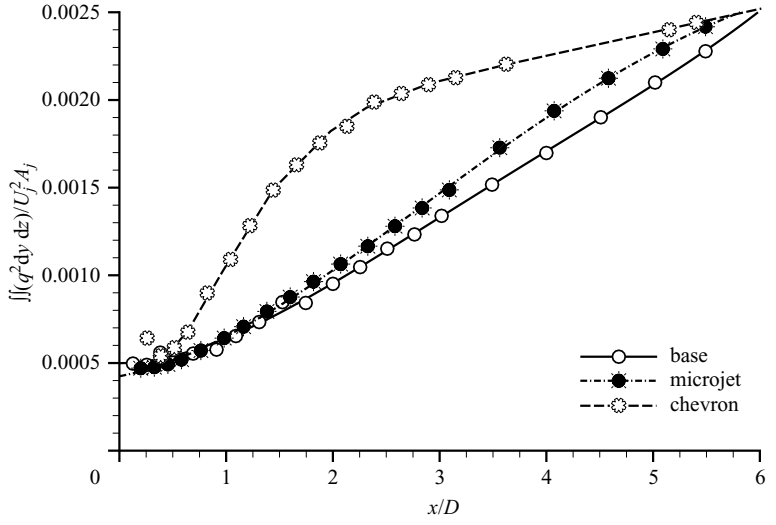

FIGURE 32. Axial variation of total TKE.

figure 23(*b*), chevrons approach a lower value than either the base or the microjet case.

The axial variation of total TKE contained in each cross-section is given in figure 32 as calculated by the integral $\int\int q^2 \,\mathrm{d}y\,\mathrm{d}z$ normalized by U_j^2 and nozzle exit area A_j. In the region $0.5 < x/D < 2$, the chevron TKE production rate is very large. Beyond $x/D = 2$, the chevrons assume a much lower rate than the other cases. Microjets show slightly increased total TKE values, but the rate of production falls below the base case beyond $x/D = 4$. The value of total TKE at $x/D = 6$ becomes the same for all cases.

These observations suggest that the additional streamwise vorticity generated by either microjets or chevrons disrupts the natural coherence of the initial layer and alters the distribution of ω_θ and associated shear stresses. It is also clear that ω_x directly increases entrainment, shear-layer growth, and ultimately the production of turbulent kinetic energy. Considering the data including other axial locations where $x/D < 2$, it can be observed that the location of the peak turbulent kinetic energy is between vortex pairs: on the low-speed side of the shear layer for the microjet case and on the high-speed side for the chevrons. The effect of initial vortex strength is

also evidenced by the larger changes in mean and turbulent flow parameters produced by the chevrons.

4. Summary and conclusions

The effect of the streamwise vortices on the aeroacoustics of a Mach 0.9 axisymmetric jet has been investigated using flow fields representative of chevron and microjet noise-reduction devices. Although the devices are not current state-of-the-art designs, they accentuate the flow-field characteristics they are producing, such that the differences and similarities can be detected more easily. As such, microjets used here are acoustically much closer to the optimum design than the chevrons are.

Acoustic field measurements show a reduction of noise level at low frequencies for both cases. The reduction in levels of the low-frequency spectrum content can be attributed to a diminished growth in the large-scale coherent structures at the jet exit. However, increased mixing generates small scales which rapidly dissipate, increasing the high-frequency SPL content. For example, the relatively greater high-frequency content in the chevron case is consistent with the increased mixing and jet spreading observed in flow-field measurements. The resulting acoustic directivity curve shows that the measured OASPL for the chevron nozzle is reduced only in the aft quadrant at angles $>130^{\circ}$, whereas the microjet injection is effective at all angles. The differences observed in OASPL behaviour owing to the two methods can be explained by considering the different scales of flow structures in the shear layer. The noise radiated in the peak noise direction is dominated by the large-scale coherent structures, whereas in the upstream direction, e.g. 90°, the noise radiation is dominated by the fine-scale structures (Tam 1995). Consequently, the change in different turbulence scales can be inferred from the acoustic spectra.

Noise maps obtained from the acoustic phased array support these data. The phased array also reveals that sources of almost every frequency move upstream, particularly for the chevron case. One exception is the low-frequency sources for the microjet case which shows a slight shift in the downstream direction. These observations correspond to changes in the jet core lengths and correlate well with other experimental observations. An increase in core length due to microjets is reported in various studies (Arakeri *et al.* 2003; Krothapalli *et al.* 2003; Alkislar *et al.* 2005) and the shortening of the core by chevrons is discussed in Bridges & Wernet (2002). At high frequencies, both methods shift the peak sources upstream. Microjets shift the curve $1D$ upstream without affecting the peak values. In contrast, chevrons greatly foreshorten the profile, shift the peak upstream about $2D$, and increase the peak intensity.

The influence of streamwise vorticity can be inferred from the PIV data. In this work, it has been directly related to increases in initial shear-layer entrainment, turbulent shear stresses, and ultimately, the production of turbulent kinetic energy. Both microjets and chevrons influence the mean axial velocity profiles, changing the magnitude and location of the peak azimuthal vorticity in the shear layer. Microjet injection decreases the peak value and hence has a stabilizing effect. In contrast, the chevron peak value is shifted to the high-speed side of the shear layer and the velocity profile becomes unstable.

Measured changes in turbulent kinetic energy levels produced by increases in axial vorticity correspond to observed changes in the acoustic field. The near-field flow characteristics obtained by means of stereoscopic PIV reveal that, relative to the base case, both chevrons and microjets increase turbulence levels in the initial shear layer.

The result is a reduction in jet noise at low frequencies and an increase at higher frequencies. The magnitude of high-frequency lift has been directly related to increases in high-frequency emission and initial vortex strength, suggesting that increased entrainment promotes the generation of small scales. This observation is supported by the work of Foss & Zaman (1999) where it was shown that the small-scale eddy population increased with vortex strength and eddy fluctuations shifted to higher frequencies (from 3.1 kHz to 4.2 kHz at 45° immersion) with the application of a chevron. Our measurements show that the turbulent quantities peak at an axial location of about $x/D = 2$, correlating with the location of peak high-frequency noise sources.

As compared to the base case, chevrons produce 30 % more turbulence in magnitude in the initial layer relative to the base case, with peak values occurring on the high-speed side of the shear layer. Microjets, on the other hand, increase turbulence levels by at most 10 %, favouring the low-speed side of the shear layer. It is hypothesized that the location of these turbulence fluctuations are critical to the generation and increase of high-frequency noise. The measured differences in the magnitude of the high-frequency lift appear to be related to the peak turbulent kinetic energy. This, in turn, is reflected in the OASPL directivity.

The location, strength and persistance of streamwise vorticity directly affect jet aeroacoustics. These results suggest that (i) the streamwise vortex should only be strong enough to disrupt the generation of azimuthally coherent large-scale structures, (ii) the streamwise vortices should be generated such that if any additional turbulent kinetic energy is produced it should be targeted mostly on the low-speed side, and (iii) optimums may exist for the initial strength and separation of streamwise vortices.

Financial and facility support from Boeing Company and ONR is gratefully acknowledged.

Appendix A. Determination of the coordinate system and rotation to the cross-plane

The origin of the coordinate system is considered to be the origin of the symmetric mean jet profile. The velocity centroid along the jet axis is found from the measured axial mean velocity profile as

$$\bar{y} = \frac{\sum_i \sum_j u_{i,j} y_{i,j}}{\sum_i \sum_j u_{i,j}}, \qquad \bar{z} = \frac{\sum_i \sum_j u_{i,j} z_{i,j}}{\sum_i \sum_j u_{i,j}}$$

and assigned as the origin.

In the next step, as defined in figure 33(*a*), the angles of rotation are found from the measured mean velocity vector components ($\boldsymbol{u} = \boldsymbol{u}(u, v, w)$) at the origin by

$$\phi = \arctan\left(\frac{-v}{\sqrt{u^2 + w^2}}\right), \qquad \psi = \arctan\left(\frac{w}{u}\right),$$

where angles ψ and ϕ represent the rotation of vectors around the y and z unit vectors, respectively. Once the angles are determined, they are used to form the rotational transformation matrices,

$$\boldsymbol{R}_\psi = \begin{bmatrix} \cos\psi & 0 & -\sin\psi \\ 0 & 1 & 0 \\ \sin\psi & 0 & \cos\psi \end{bmatrix}, \quad \boldsymbol{R}_\phi = \begin{bmatrix} \cos\phi & -\sin\phi & 0 \\ \sin\phi & \cos\phi & 0 \\ 0 & 0 & 1 \end{bmatrix}, \quad \boldsymbol{R} = \boldsymbol{R}_\phi \boldsymbol{R}_\psi$$

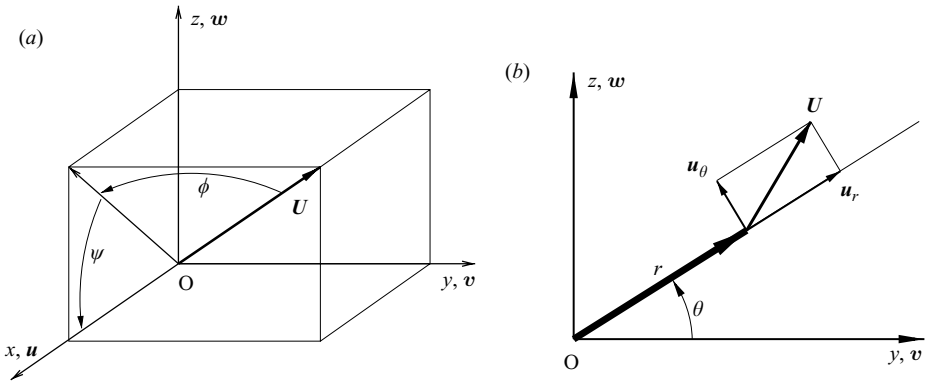

FIGURE 33. The definition of (*a*) Cartesian and (*b*) cylindrical coordinates.

The total rotation matrix $\boldsymbol{R}$, is in turn used to transform the velocity vector and the turbulence tensor $\boldsymbol{S}'$ at each point in the plane.

$$\boldsymbol{u}_T = \boldsymbol{R}\boldsymbol{u}, \qquad \boldsymbol{S}'_T = \boldsymbol{R}\boldsymbol{S}'\boldsymbol{R}^T, \qquad \boldsymbol{S}' = \begin{bmatrix} \overline{u'^2} & \overline{u'v'} & \overline{u'w'} \\ \overline{u'v'} & \overline{v'^2} & \overline{v'w'} \\ \overline{u'w'} & \overline{v'w'} & \overline{w'^2}. \end{bmatrix}.$$

Appendix B. Representation of the stress tensor in the cylindrical coordinates

The transformation angle is defined at each point in the measurement plane (figure 33*b*) with the resultant velocity vector, $\boldsymbol{u}_c$ and turbulent stress tensor, $\boldsymbol{S}'_c$, calculated by

$$\theta = \arctan\left(\frac{z}{y}\right), \ \boldsymbol{R}_x = \begin{bmatrix} 1 & 0 & 0 \\ 0 & \cos\theta & \sin\theta \\ 0 & -\sin\theta & \cos\theta \end{bmatrix}, \ \boldsymbol{u}_c = \boldsymbol{R}_x\boldsymbol{u}_T, \ \boldsymbol{S}'_c = \boldsymbol{R}_x\boldsymbol{S}'_T\boldsymbol{R}_x^T.$$

The resultant components of symmetric turbulent stress tensor $\boldsymbol{S}'_c$, are given by the following equations,

$$\begin{aligned} \overline{u'^2_x} &= \overline{u'^2}, \\ \overline{u'^2_r} &= \overline{v'^2}\cos^2\theta + \overline{w'^2}\sin^2\theta + \overline{v'w'}\sin 2\theta, \\ \overline{u'^2_\theta} &= \overline{v'^2}\sin^2\theta + \overline{w'^2}\cos^2\theta - \overline{v'w'}\sin 2\theta, \\ \overline{u'_x u'_r} &= \overline{u'v'}\cos\theta + \overline{u'w'}\sin\theta, \\ \overline{u'_x u'_\theta} &= -\overline{u'v'}\sin\theta + \overline{u'w'}\cos\theta, \\ \overline{u'_r u'_\theta} &= \tfrac{1}{2}(\overline{u'^2} - \overline{w'^2})\sin 2\theta + \overline{u'w'}\cos 2\theta, \end{aligned}$$

where the subscripts denoted by x, r and θ represent, respectively, the axial, radial and azimuthal components of the velocity vector.

REFERENCES

ALKISLAR, M. B., LOURENCO, L. M. & KROTHAPALLI, A. 2000 Stereoscopic PIV measurements of a screeching supersonic jet. *J. Visualization* **3**, 135–143.

ALKISLAR, M. B., KROTHAPALLI, A. & LOURENCO, L. M. 2003 Structure of a screeching rectangular jet: a stereoscopic PIV study. *J. Fluid Mech.* **489**, 121–154.

ALKISLAR, M. B., KROTHAPALLI, A., CHOUTAPALLI, I. & LOURENCO, L. M. 2005 Structure of supersonic twin jets. *AIAA J.* **43**, 2309–2318.

Arakeri, V. H., Krothapalli, A., Siddavaram, V., Alkislar, M. B. & Lourenco, L. M. 2003 On the use of microjets to suppress turbulence in a Mach 0.9 axisymmetric jet. *J. Fluid Mech.* **490**, 75–98.

Bohl, D. & Foss, J. F. 1999 Near exit plane effects caused by primary and primary-plus-secondary tabs. *AIAA J.* **37**, 192–201.

Bridges, J. & Brown, C. A. 2004 Parametric testing of chevrons on single flow hot jets. *AIAA Paper* 04-2824.

Bridges, J. & Wernet, M. P. 2002 Turbulence measurements of separate flow nozzles with mixing enhancement features. *AIAA Paper* 02-2484.

Bridges, J., Wernet, M. P. & Brown, C. A. 2003 Control of jet noise through mixing enhancement *NASA TM* 2003-212335.

Brown, G. L. & Roshko, A. 1974 On density effects and large structures in turbulent mixing layers. *J. Fluid Mech.* **64**, 775–816.

Coiffet, F. 2006 Étude stochastique tridimensionnelle de la dualité des pressions en champ proche des jets axisymétriques turbulents à haut nombre de Reynolds. PhD thesis, Université de Poitiers, France.

Cortelezzi, L. & Karagozian, A. T. 2001 On the formation of the counter-rotating vortex pair in transverse jets. *J. Fluid Mech.* **446**, 347–373.

Crighton, D. G. 1981 Acoustics as a branch of fluid mechanics. *J. Fluid Mech.* **106**, 261–298.

Crow, S. C. & Champagne, F. H. 1971 Orderly structure in jet turbulence. *J. Fluid Mech.* **48**, 547–591.

Eroglu, A. & Breidenthal, R. E. 2001 Structure, penetration, and mixing of pulsed jets in crossflow. *AIAA J.* **39**, 417–423.

Foss, J. K. & Zaman, K. B. M. Q. 1999 Large- and small-scale vortical motions in a shear layer perturbed by tabs. *J. Fluid Mech.* **382**, 307–329.

Fric, T. F. & Roshko, A. 1994 The structure in the wake of a transverse jet. *J. Fluid Mech.* **279**, 1–47.

Greska, B., Krothapalli, A., Seiner, J., Jansen, B. & Ukeiley, J. 2005 The effects of microjet injection on an F404 jet engine. *AIAA Paper* 2005-3047.

Hasselbrink Jr, E. F. & Mungal, M. G. 2001 Transverse jets and jet flames. Part 1. Scaling laws for strong transverse jets. *J. Fluid Mech.* **443**, 1–25.

Johari, H. & Rixon, G. 2003 Effects of pulsing on a vortex generator jet. *AIAA J.* **41**, 2309–2315.

Kelso, R. M., Lim, T. T. & Perry, A. E. 1996 An experimental study of round jets in cross-flow. *J. Fluid Mech.* **306**, 111–144.

Krothapalli, A., Greska, B. & Arakeri, V. 2002 High-speed jet noise reduction using microjets. *AIAA Paper* 2002-2450.

Krothapalli, A., Choutapalli, I., Alkislar, M. B. & Lourenco, L. M. 2003 Aeroacoustics of twin supersonic impinging jets. *AIAA Paper* 2003-3316.

Krothapalli, A., Arakeri, V. & Greska, B. 2004 Mach wave radiation: a review and an extension. *AIAA Paper* 2004-1200.

Lourenco, L. M. & Krothapalli, A. 2000 True resolution PIV: a mesh-free second-order accurate algorithm. *Proc. 10th Intl Symp. on Applications of Laser Techniques in Fluid Mechanics.*

Moore, C. J. 1977 The role of shear-layer instability waves in jet exhaust noise. *J. Fluid Mech.* **80**, 321–367.

NACA 1953 Equations, tables, and charts for compressible flow. *NACA Rep.* pp. 1–69.

Opalski, A. B., Wernet, M. P. & Bridges, J. E. 2005 Chevron nozzle performance characterization using stereoscopic PIV. *AIAA Paper* 2005-0444.

Peterson, S. D. & Plesniak, M. W. 2004 Evolution of jets emanationg from short holes into crossflow. *J. Fluid Mech.* **503**, 57–91.

Saiyed, N. H., Mikkelsen, K. L. & Bridges, J. E. 2003 Acoustics and thrust of quiet separate-flow high-bypass-ratio nozzles. *AIAA J.* 372–378.

Tam, C. K. W. 1995 Supersonic jet noise. *Annu. Rev. Fluid Mech.* **27**, 17–43.

Underbrink, J. R. 2001 Circularly symmetric, zero redundancy, planar array having broad frequency range application. US Patent No. 6 205 224 2001.

Underbrink, J. R. 2002 Aeroacoustic phased array testing in low speed wind tunnels. In *Aeroacoustic Measurements* (ed. T. L. Mueller). Springer.